Sensor and Simulation Notes

Note 265

December 1979

An Experimental Investigation of the King Surface Current Probing Technique in a Transient Application

L. Wilson Pearson
Youn M. Lee

University of Kentucky
Lexington, Kentucky

Abstract

An experimental technique to measure transient surface currents of a scatterer using a King-type semicircular miniature probe is reported. The principal extension of the King technique is the use of the loop probe in transient currents measurement. The transient characteristics of the probe are considered based on the Whiteside theory [29] for the loop. The probes fabricated were subjected to transient excitation in a coaxial calibration jib. Their frequency responses were determined by Fourier transforming their output and deconvolving the excitation spectrum. The agreement between the measured results and the Whiteside theory is observed and evaluated. The probe geometry was tested in an application context, namely, the probing of current on a cylindrical scatterer. The induced surface currents were measured using the probe along the scatterer, and deconvolution of the probe transfer function was carried out subsequently. The deconvolved waveforms are reported and the results of numerical predictions by way of a time domain integral equation technique are reported for comparison. The application goal for this work lies in the numerical extraction of the Singularity Expansion Method (SEM) description of scattering from a given object, using measured transient data. The extraction process was carried out on the cylindrical scatterer data. The results reported here point to the feasibility of this procedure. Implications of extending the probing method for complex-shaped objects are discussed.

Acknowledgements

The authors are grateful to Mr. A. S. Hebert for his able assistance in the construction of the transient range and the models used in this work. Mr. J. R. Auton carried out the extraction of the SEM description reported here. The Harrison and King model for the incident field used in the TWTD computations was computed and validated by Mr. B. Wade. Mr. G. B. Melson developed the data acquisition software for the measurement system. Mrs. Betty Bradshaw and Mr. J. DesRosiers did the manuscript preparation.

Sensor and Simulation Notes

Note 265

December 1979

An Experimental Investigation of the King Surface Current Probing Technique in a Transient Application

L. Wilson Pearson
Youn M. Lee

University of Kentucky
Lexington, Kentucky

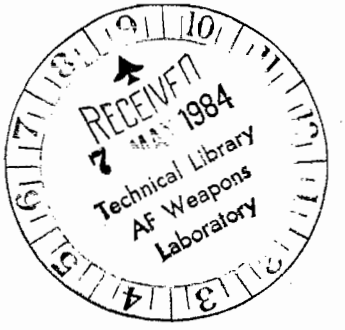

Abstract

An experimental technique to measure transient surface currents of a scatterer using a King-type semicircular miniature probe is reported. The principal extension of the King technique is the use of the loop probe in transient currents measurement. The transient characteristics of the probe are considered based on the Whiteside theory [29] for the loop. The probes fabricated were subjected to transient excitation in a coaxial calibration jib. Their frequency responses were determined by Fourier transforming their output and deconvolving the excitation spectrum. The agreement between the measured results and the Whiteside theory is observed and evaluated. The probe geometry was tested in an application context, namely, the probing of current on a cylindrical scatterer. The induced surface currents were measured using the probe along the scatterer, and deconvolution of the probe transfer function was carried out subsequently. The deconvolved waveforms are reported and the results of numerical predictions by way of a time domain integral equation technique are reported for comparison. The application goal for this work lies in the numerical extraction of the Singularity Expansion Method (SEM) description of scattering from a given object, using measured transient data. The extraction process was carried out on the cylindrical scatterer data. The results reported here point to the feasibility of this procedure. Implications of extending the probing method for complex-shaped objects are discussed.

probes, loops, surface currents, SEM (singularity expansion mode), predictions, spectra, waveforms

Acknowledgements

The authors are grateful to Mr. A. S. Hebert for his able assistance in the construction of the transient range and the models used in this work. Mr. J. R. Auton carried out the extraction of the SEM description reported here. The Harrison and King model for the incident field used in the TWTD computations was computed and validated by Mr. B. Wade. Mr. G. B. Melson developed the data acquisition software for the measurement system. Mrs. Betty Bradshaw and Mr. J. DesRosiers did the manuscript preparation.

TABLE OF CONTENTS

LIST OF FIGURES

Page

I. INTRODUCTION

1.1 Transient Probing Problem

The principal goal of the work reported here is the development of a surface current probing technique which is usable on a transient (broadband) basis. The probing scheme is to be used ultimately in the extraction of the Singularity Expansion Method (SEM) descriptions of complex-shaped scatterers through experimental means as described in Reference [1].

As reported in [1], it is feasible to measure transient surface current response at many points on a scattering object under study or a model thereof, even when the object is so complex as an aircraft. Figure 1 pictures the generic configuration of the measurement which is used to derive transient surface current waveforms. The object is suspended in the presence of a radiating transient field produced by a transient signal source and a transmitting antenna. For SEM extraction purposes the accurate characterization of this field at the scattering object is an important prerequisite for the experimental configuration. For present purposes this is a secondary consideration. The surface current on the object is probed through a multiplicity of miniature surface current probes, indicated by the small arrows in Figure 1. Each of these probes provides a transient output signal when the object is excited. Typically, magnetic loop probes provide a voltage response which is proportional to the time

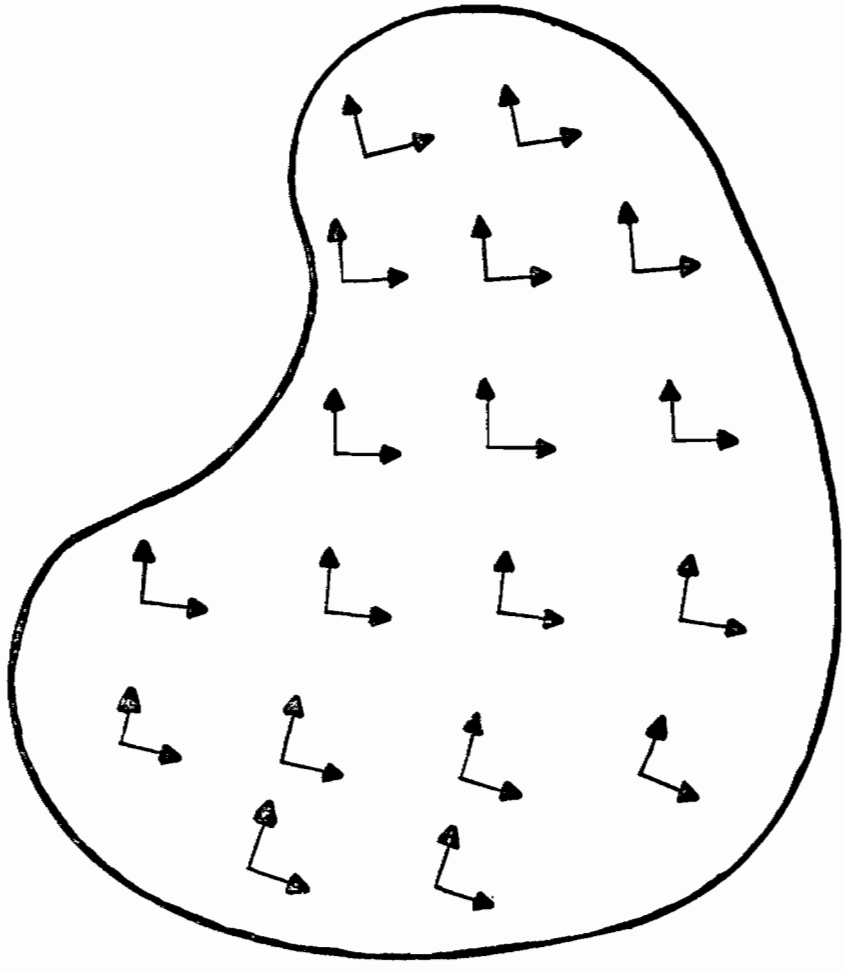

Figure 1. Generic configuration for the measurement of the current waveforms.

derivative of the current flowing in the probed direction at the sample location. The present work seeks to explicitly define the realization of these probes and to establish the methodology of their application.

Transient probing is, at times, tedious to carry out, but advantages result relative to continuous-wave (CW) analysis. In particular, we can determine the object's response over a broad range of frequency by using transient techniques. The work reported in [1] describes a method whereby one can derive the SEM description of an object by means of probed transient response data. The Singularity Expansion Method enables us to analyze the transient coupling in such a way as to understand it better and to represent it compactly. The SEM representation is quite powerful in data reduction and can be used to predict the response of the object regardless of direction and time history (within band limitations) of the incident wave. One can extract the natural resonances and associated modes of the object from which the scattering response may be expanded for new excitations -- transient or CW.

The experimental method to determine transient electromagnetic coupling to metallic objects demands careful consideration of the probing technique used in measuring the electric field or the magnetic field. A field probe should be designed such that it senses the field quantity of interest and is insensitive to other field quantities. Typically, it should be characterizable as electrically small in the frequency range of interest so that conventional circuit analysis can be carried out without too much complexity.

1.2 Ground Plane Considerations

One must consider eliminating or minimizing the effect of couplings between the object under study and other bodies such as measurement instruments and transmission cables. Utilization of the ground plane technique is a way of avoiding these problems. To do so imposes a limitation, however [1]. Namely, only half of the modes on the object being imaged are antisymmetric with respect to the symmetry plane. The modes which are symmetric with respect to the symmetry plane are not recoverable through the ground plane measurement.

1.3 Brief Survey of Miniature Probes

A great deal of work has been carried out in the EMP community in the development of the electric field and/or magnetic field sensors--so-called D-dot sensors and B-dot sensors, respectively. Most of the sensors described below were developed for full scale aircraft measurements.

R. E. Partridge at the Los Alamos Scientific Laboratory has developed an "invisible" absolute E-field probe which creates a minimum of disturbance to the field in its vicinity and has a calculable absolute sensitivity [2]. He uses this idea in modifying the rectangular loop to measure the E-field and H-field simultaneously by employing a common mode amplifier and a differential amplifier [3]. Orsak and Whitson reported utilization of a capacitive electric field sensor developed by C. T. R. Wilson. That sensor was made in the form of an asymmetric plate to house a preamplifier including the battery and switch. This probe is 4 inches in diameter and stands

3.25 inches high [4]. Use of an asymmetric dipole made of coaxial transmission line as a transient probe was discussed by Hall [5]. Baum has described twenty-one other probe configurations of importance [6-26]. A current-sampling vertical current density sensor and inductively-coupled vertical current density sensor were developed for the purpose of measuring the vertical component of the total current density at a soil or water surface [6]. A discussion about the design of electrically-small multi-turn cylindrical loops in the measurement of inhomogeneous magnetic fields and inductance can be found in Reference [7]. Design and analysis of inductive current sensors which measure the line integral of the magnetic field around an area of interest by using an appropriate array of conducting loops was reported in [8]. An analysis of the circular flush-plate dipole in nonconducting media was carried out. This sensor was analyzed using the cylindrical vector eigen-function expansions [9]. The moebius strip loop has improved upon the conventional coaxial loop in some applications. It has the properties of doubled sensitivity to the magnetic field but much less sensitivity to transient radiation effects [10]. A maximization frequency response of the B-dot loop was examined. Four limitations are considered for the B-dot loop. These can be summarized as the loop radius, the matching of the impedances of the equivalent transmission line of the loop, and the size of the structure [11]. An investigation of detecting electric fields in a dissipative media can be found in Reference [12]. A sensor (which has flat frequency response) was developed to measure the electric field in such a medium. A possibility of designing a probe so that it can sense the electric field

associated with the close-in EMP has been investigated. Certain constraints in building such a probe are reported in Reference [13], as well. Development of a technique for measuring electric fields with internal EMP using wire grids can be found in Reference [14]. A generalization of the moebius strip loop is reported for measuring magnetic fields [15]. The effects of radiation and conductivity on a B-dot loop design consideration is considered in Reference [16]. Calculations of the frequency response characteristics of the cylindrical loop are carried out for both nonconducting and conducting media for two types of cylindrical loop design [17]. Some various sensor parameters are defined for electrically-small loops and dipoles following equivalent circuits considerations [18]. Multi-gap cylindrical loop response characteristics when immersed in the nonconducting media have been reported [19]. Some design parameters are considered for a pulse-radiating dipole antenna as associated with the high-frequency and low-frequency content of the radiated waveform [20]. Reference [21] provides a technique through which one can define the geometry of a dipole antenna such that low-frequency parameters of the antenna are readily calculable. Some electrical parameters of loop sensors for measuring the magnetic field perpendicular to the cylinder axis are reported in Reference [22]. An analysis of a dipole with two parallel conducting plates, one of the common sensors for measuring an electric field, is reported for the case of two equal conducting plates [23]. Further considerations of this circular parallel-plate dipole can be found in Reference [24]. Reference [25] describes an analysis of a resistively-loaded dipole antenna for which the resistance is continuously distributed along

the antenna such that resistance loading is in series with the antenna conductors. The response of a hollow spherical dipole in nonconducting media is considered in Reference [26]. This spherically-shaped sensor with a slot around the equator is uniformly resistively-loaded.

Most of the probes developed by the EMP community are large in size. For small-scale objects such as ours, they cannot be scaled so as to be electrically-small. It will be extremely difficult, if not impossible, to fabricate these probes when scaled down in size since they typically involve several pieces and intricate shapes. Scaling these configurations to a small size introduces severe complications regarding the reproducibility of the probes. Current and charge probes have been implemented on a relatively small scale by EG & G for the Air Force Weapons Laboratory.* These implementations are costly if considered in a multiple-probe context, such as in Figure 1, and are too large by approximately a factor of two for the scale of models which are convenient for indoor transient measurements.

R. W. P. King and his protégés have developed a miniature magnetic field current probe and thoroughly analyzed its characteristics on a CW basis [27]. In analyzing the magnetic probe, which takes the form of a small circular or rectangular loop, they considered two dominant mode currents which the finite loop sustains: namely, the transmission line mode current and the dipole mode

*Model ACD-1A(R) D-dot and Model MGL-8B(R) B-dot probes manufactured by EG & G, Albuquerque, NM.

current. The transmission line mode current is proportional to the magnetic field passing through the loop, and the dipole mode current senses an electric field component in the plane of the loop. By properly choosing the load point, they eliminate the contribution of the dipole mode to the load voltage.

1.4 Motivation for Adopting King Probe in Transient Application

The "King-type" loop probes described in [27] are well-suited to the present application. The following features are important to the multiple-probe transient measurement configuration:

1. The probe must be implementable in a small size (nominally 0.100-0.200 inches diameter);
2. The probe must be low in electrical loss for the sake of sensitivity;
3. The probe and its transmission system must be nonresonant over a broad bandwidth, and its frequency response must be characterized for deconvolution purposes;
4. The fabrication must be reproducible; and
5. The fabrication process must be reasonably economical in the multiple-probe context.

The first of these requirements is readily met if the probe is fabricated from miniature semi-rigid coaxial cable of either 0.023 inch or 0.033 inch diameter. Concomitantly, the fabrication procedure involves a few steps and simple tooling. Thus, points 4. and 5. above are honored, as well.

The King designs described in [27] incorporate an electrical junction interior to the probe body where the loop center conductor joins the cable leading the measured signal away from the probe. This junction manifests local reactance and, thereby, the possibility for undesirable resonances. At the least, this reactance will

introduce its own frequency response to that of the probe assembly. We circumvented this difficulty by fabricating the probe loop and its signal cable from a single continuous piece of semi-rigid cable.* This configuration leads to the honoring of requirement 3. above. While the King design introduces no intentional loss into the probe assembly, the continuous cable configuration requires a single cable which is small in diameter. The loss of even a fraction of a meter of such cable manifests appreciable loss at the upper end of the spectrum of interest. This loss is tolerable in terms of sensitivity, but it must be accounted for in the frequency-response calibration of the probe.

1.5 Survey of the Present Work

This work describes the results of adopting the King-type probe for transient measurement. Chapter 2 presents the chosen implementation of the current probe. The configuration is described in detail and the theoretical performance is predicted in terms of the development in [27]. A calibration fixture suitable for experimentally calibrating probes to be used on a cylindrical surface is described. A measured calibration is presented and compared with the theoretical predictions.

The probe scheme has been implemented on a cylindrical scatterer in order to assess its viability. The cylindrical object was chosen because its transient response is well-characterized and because the movable probe methods described in [27] can be

*Liepa has independently developed a similar scheme for broadband CW measurements [28].

applied. Chapter 3 describes this implementation and presents the significant results obtained. These results include SEM mode extractions.

Chapter 4 draws conclusions from the present work and suggests the application and usage of the current probe. The Appendix portrays details of the fabrication technique of a current probe.

II. IMPLEMENTATION OF LOOP PROBES

2.1 Introduction

This section describes the details of the implementation of the King-type loop probe for measurement of transient currents induced on a thin cylindrical scatterer. The cylindrical scatterer was chosen for an initial study of the use of loop probes in transient SEM extraction because its SEM description is already well-known and because it is amenable to a sliding probe configuration, therby avoiding, initially, the need for multiple probes.

In the following, the specific mechanical configuration of the probes used in this work is described. The basis for theoretically predicting their response is described and ultimately compared with measured frequency response derived through a transient measurement. The coaxial jig used to expose the probe to a known field is described, as well.

2.2 Construction Form

The fundamental problem faced in applying King's technique to transient measurements is that the transmission line system must be well-matched from the probe output to the load. In the present case, the input of the oscilloscope which samples the waveform is the load. Any severe mismatches would introduce resonances into the measurement system frequency response. These resonances would limit the accuracy with which the probe response could be deconvolved from the measured waveform.

In this work, 0.023 inch diameter, 50 ohm, semi-rigid coaxial cable was used to construct the probe as shown in the cross section view in Figure 2a. The transmission line leading from the probe and the probe itself are made of one piece of coaxial cable, thus directly eliminating most sources of mismatch. The probe is semicircular with a load-gap at the center of the semicircular loop and is mounted on a cylindrical carriage. The transmission line is secured in 1/16 inch hollow brass tubing. The cylindrical carriage conforms to the inside diameter of the tubing from which the cylindrical scatterer is fabricated. The carriage can slide in a notched tube so that a single probe can observe the current flowing at any location along the scatterer. The 1/16 inch protective tube serves a second function as the pushrod for this carriage. Figure 2b shows a closeup photograph of a probe assembly. Figure 3a shows the same probe assembly residing in the slot in a cylindircal scatterer mode. Figure 3b shows the probe in the scatterer after the slot has been covered with conducting tape to block its influence from the measurement. Details of the construction technique can be found in the Appendix.

To our knowledge, no connector is commercially available which can directly accommodate 0.023 inch semi-rigid coaxial cable. A commercially available connector compatible with 0.035 inch cable was adapted using the scheme indicated in Figure 4.* Figure 5 pictures the time domain reflectometer traces of two probes

*This approach was suggested by Dr. Valdis Liepa of the Radiation Laboratory at the University of Michigan.

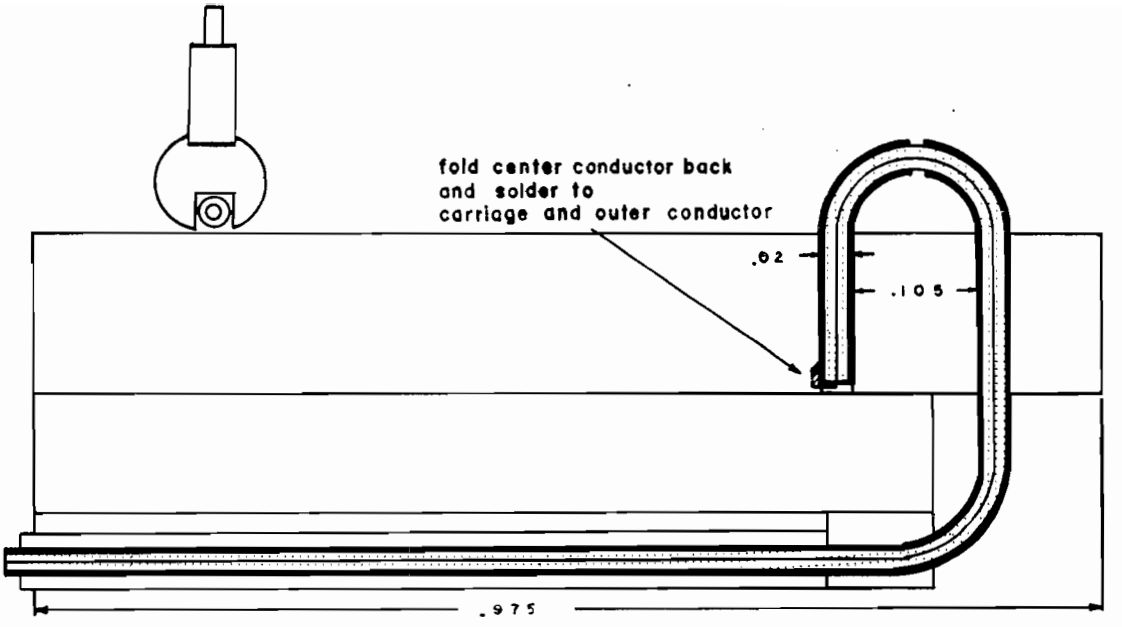

(a)

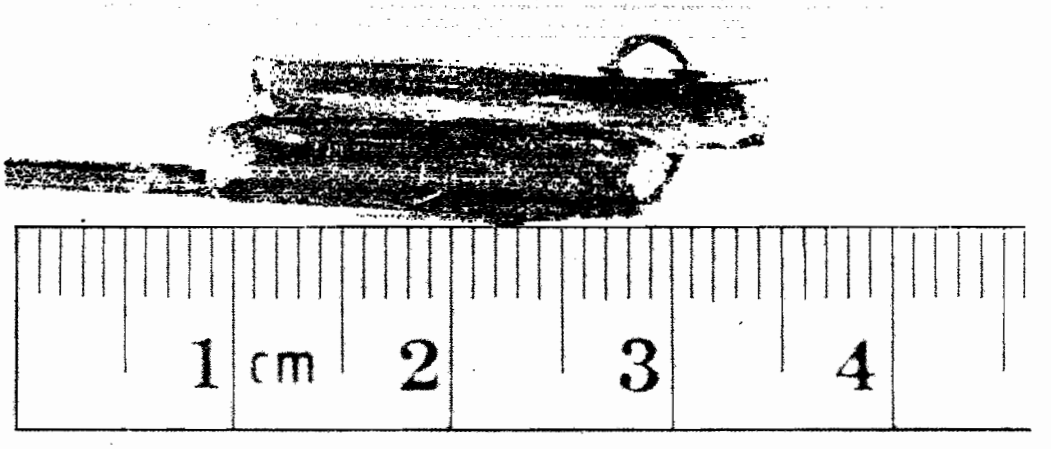

(b)

Figure 2. (a) Center cut side view and end view of the current probe mounted on a carriage.

(b) A close-up photograph of a probe assembly.

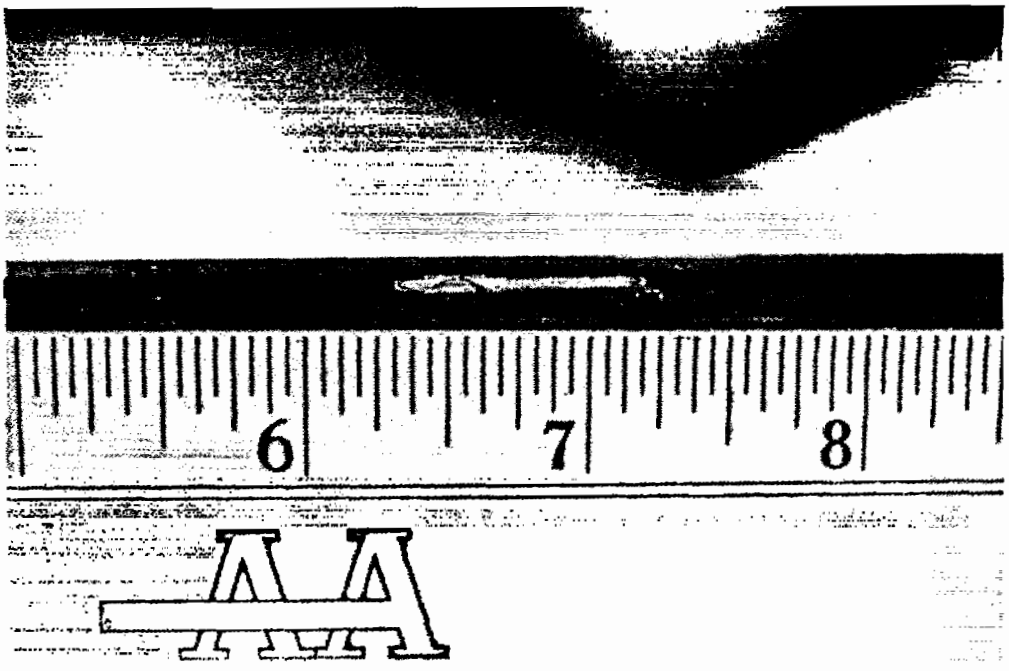

(a)

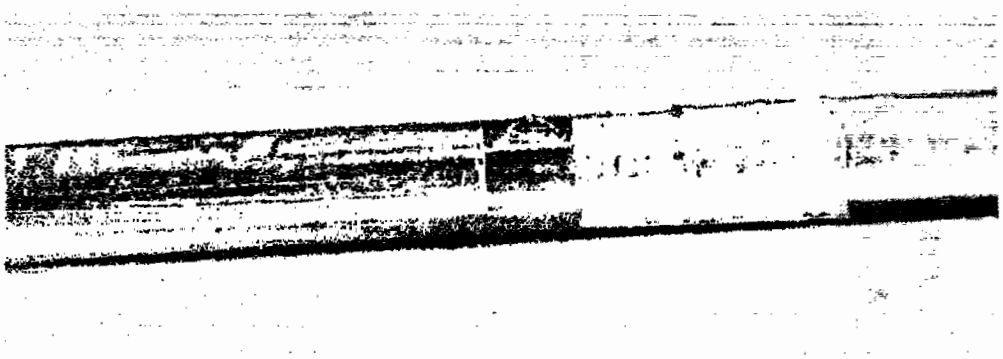

(b)

Figure 3. (a) A probe assembly fitted in the slot in a cylindrical scatterer.

(b) The probe in the scatterer after the slot has been covered with conducting tape to block its influence from the measurement.

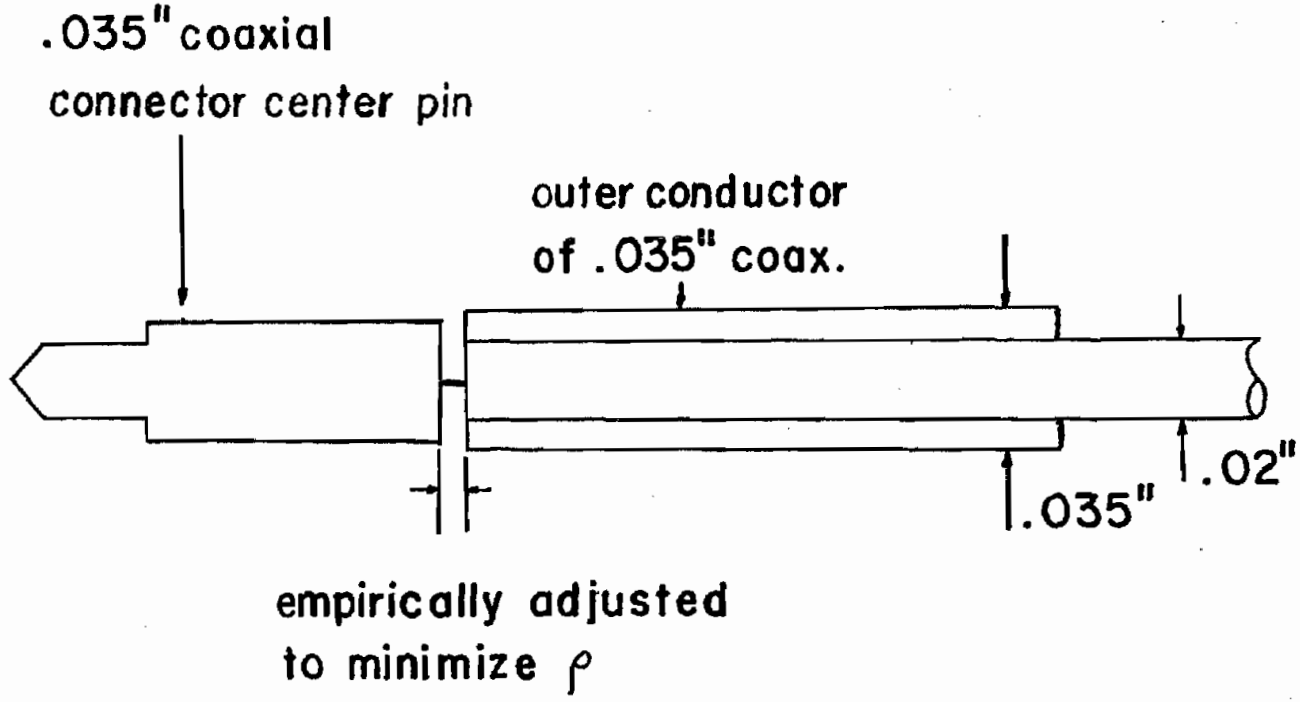

Figure 4. A method to adapt 0.035" adaptor for 0.023" coaxial cable. The assembly above fits directly into the outer conductor assembly on an Omni Spectra OSSM 551-1 connector.

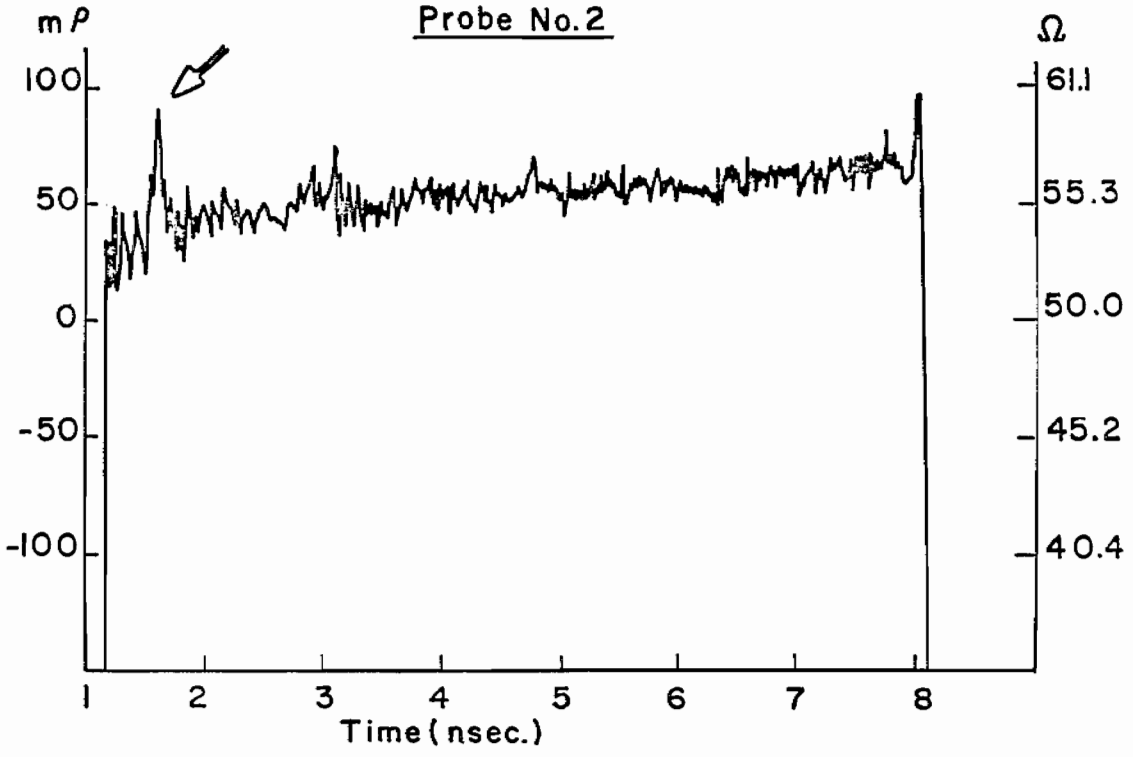

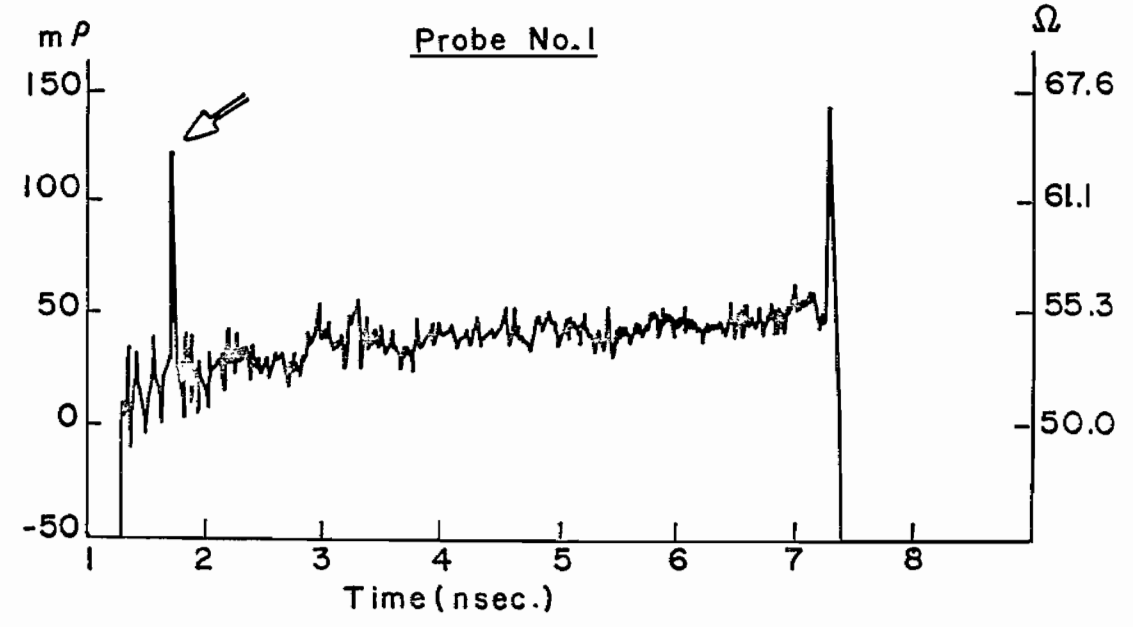

Figure 5. TDR traces of probes showing two results of empirical adjustments of gap between center pin of a 0.035" connector and 0.023" coaxial line.

through the adapted connector with the locations of center-pin gaps indicated. Probe number 1 shows some mismatch at the connector, while probe number 2 manifests a mismatch which is barely discernible from measurement noise. The sharp peak after 7 nanoseconds in both probes indicates the mismatch at the location of the notch of the probes. The source of the larger mismatch is not evident, but likely lies in fabrication differences. The measurements shown were made with a 14 GHz bandwidth TDR system. The mismatches are not appreciable over the 4 GHz bandwidth that we used in measurement.

2.3 Theoretical Analysis of the Probe Assembly

A frequency-domain analysis of our half loop, following that of Whiteside and King [29], is presented in this section for sake of completeness. Their theory is developed in the frequency domain and thus is counterpart to a Fourier transform domain theory in the present application.

Consider the semicircular receiving loop shown in Figure 6. It is loaded with impedance Z_1. Its equivalent full loop resulting from presence of a perfectly conducting image plane lying in the YZ plane is shown in the Figure, too. Of course, the loop is used on a curved surface. The approximation of a quasi-planar imaging surface is valid so long as the loop dimensions are small compared with the radius of curvature on which it is situated. Assume that the loop is symmetrical about the X and Z axes and the radius (a) of the conductor forming the loop is small so that a one-dimensional analysis of the current is adequate. The validity of this assumption is subsequently tested for the loop size used. Let $\tilde{I}_t$ represent the transmission line mode current, as indicated in

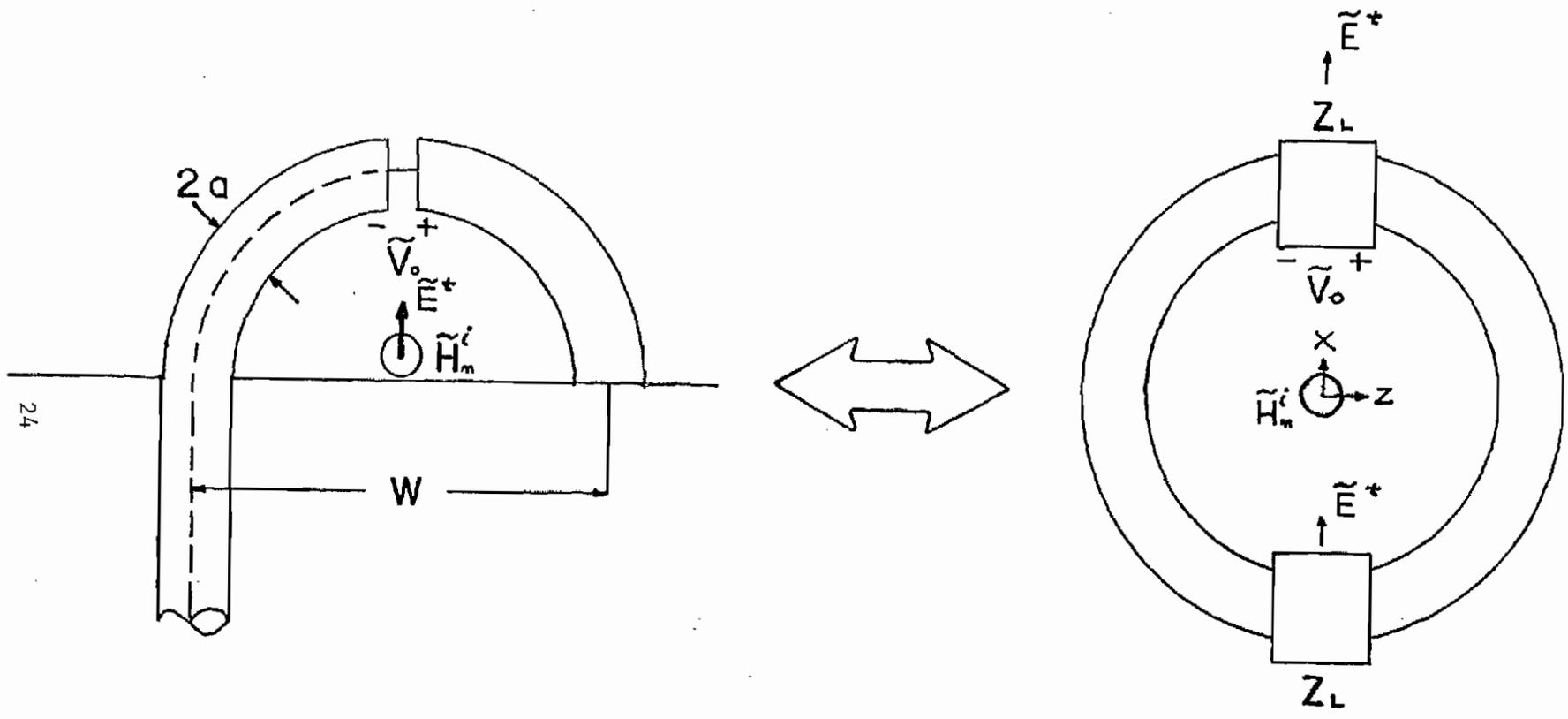

Figure 6. Geometry of loop and its equivalent block diagram.

Figure 7a.* If the loop is small compared with wavelength, $\tilde{I}_t$ can be treated as constant. The dipole mode current, $\tilde{I}_d$, is co-directional and the same on both sides of the loop, as indicated in Figure 7. Therefore, the dipole mode current must be zero at the load and, hence, does not couple into the load. The total response of the loop depends only on the transmission line mode current $\tilde{I}_t$.

It is useful to characterize the interrelation of the loop and its load by means of a Norton equivalent circuit. The admittance of the loop $\tilde{Y}_0$ is derived by Whiteside [29] using the expression given by King [30].

$$\tilde{Y}_0 = \frac{-j4}{\zeta kW(\Omega - 3.52 + 0.33(kW)^2)} ,$$

where $\zeta = 120\pi$,

$\Omega = 2 \ln(\pi W/a)$,

$k = 2\pi/\lambda$,

λ is wavelength,

and W is width of the loop as indicated in Figure 7.

Y_0 can be approximated by neglecting the $0.33(kW)^2$ term since at low frequencies the contribution of this term is very small compared with the other two terms. This allows us to view Y_0 in terms of an equivalent inductance. This inductance can be found by setting $\tilde{Y}_0 = 1/j\omega L$ and identifying $L = \zeta W(\Omega - 3.52)/4c$, where c is the speed of light. The voltage induced in the loop depends on the

*The tilde ~ denotes Fourier-transformed quantities.

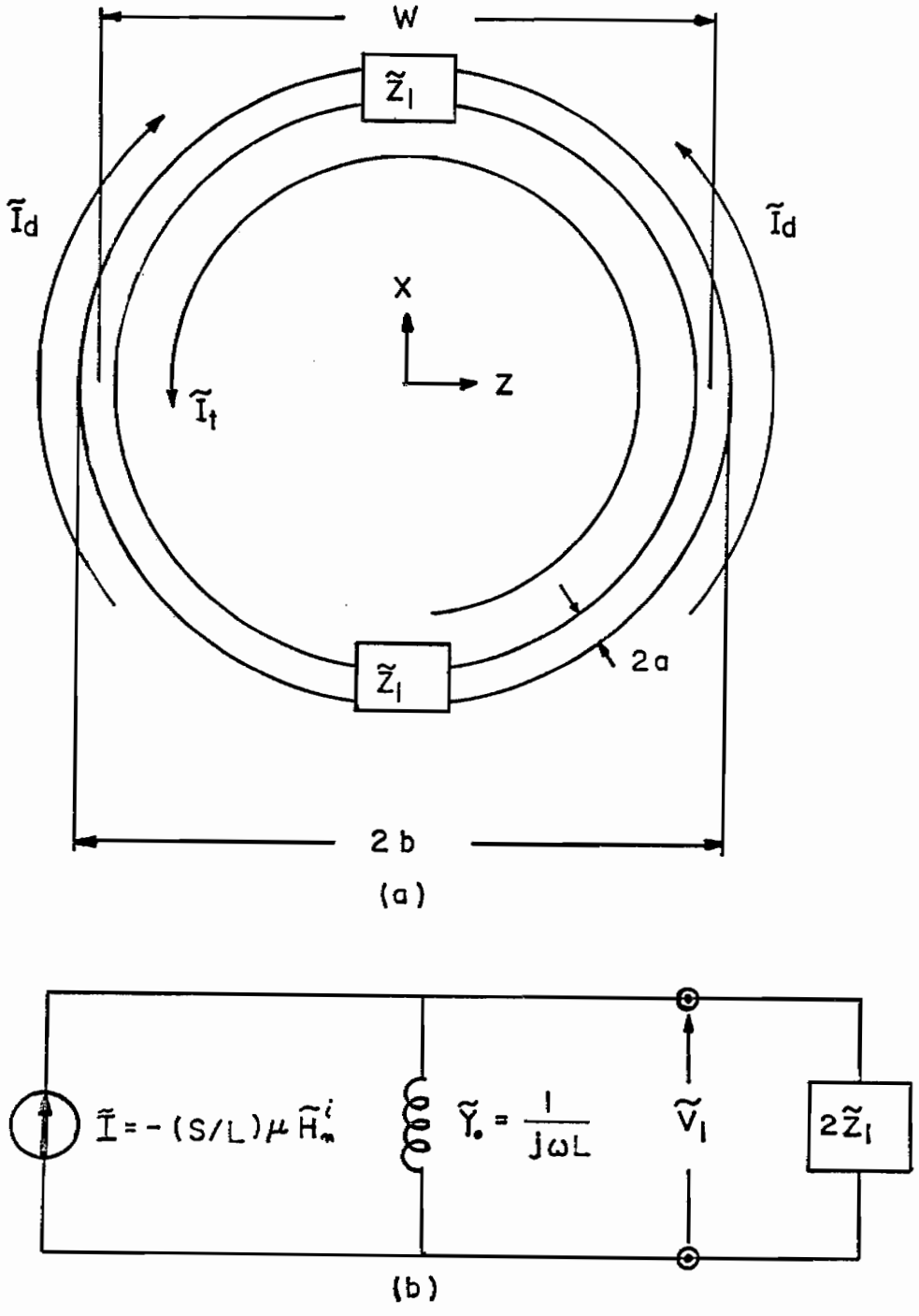

Figure 7. (a) Loop parameters are shown with transmission line mode current, $\tilde{I}_t$, and dipole mode current, $\tilde{I}_d$.

(b) An approximate circuit diagram of a circular loop.

magnetic field enclosed by the loop, according to Faraday's law

$$\tilde{V} = \oint \bar{E}\cdot d\bar{l} = -j\omega \iint \tilde{\bar{H}}\cdot d\bar{S} \ .$$

By Assuming that the magnetic field enclosed by the loop can be treated as constant over the area of the loop, the above integral can be approximated as

$$\tilde{V}(j\omega) = j\omega\mu\tilde{H}_n^i S \quad , \ \mu = 4\pi\cdot 10^{-7}$$

where S is the surface area enclosed by the loop. Thus, the no-load current in the loop can be obtained by multiplying the admittance of the loop $\tilde{Y}_0$ by the voltage $\tilde{V}$.

$$\tilde{I}(j\omega) = -j\omega S\tilde{Y}_0\mu\tilde{H}_n^i$$

$$= -(S/L)\mu\tilde{H}_n^i \ .$$

When the loop resides on a thin cylinder, the magnetic field penetrating the loop is

$$\tilde{H}_n^i = \tilde{I}_z(Z,j\omega)/2\pi r,$$

where $\tilde{I}_z(Z,j\omega)$ is the net axial current flowing on the cylinder at the probe location Z and r is the radius of the cylinder.

Now we can formulate the equivalent circuit of the doubly-loaded loop, as shown in Figure 7b. The output voltage across the load can be expressed as follows:

$$\tilde{V}_l(j\omega) = \tilde{H}(j\omega)\ \tilde{I}_z(Z,j\omega),$$

where

$$\tilde{H}(j\omega) = \frac{-\mu\tilde{Z}_1 S}{\pi r L} \cdot \frac{j\omega L}{j\omega L + 2\tilde{Z}_1} \quad . \quad (1)$$

The transfer function $\tilde{H}(j\omega)$ relates the output voltage to the current flowing on the cylinder at the probe point. For frequency components where $\omega L << 2Z_1$,

$$\tilde{H}(j\omega) \cong -j\omega\mu S/2\pi r \ .$$

This implies, in the time domain, that the loop voltage time history is proportional to the derivative of the time history of the current being probed. If the spectrum of $\tilde{I}_z(Z,j\omega)$ includes frequencies where $j\omega L$ is appreciable relative to $2\tilde{Z}_1$, then the transfer function cannot be so simply interpreted. In the measured results reported subsequently, the current spectra do include such frequencies, but these components are relatively weak. As a consequence, an approximate derivative response is observed. The original current $I_z(Z,t)$ is recoverable through deconvolution of the transfer function given in (1), or, in an approximate fashion, direct integration of the waveform.

In practice, the voltage $\tilde{V}_1$ is delivered to the oscilloscope over a length of 0.023 inch semi-rigid cable. The attenuation of this length of cable is significant. Therefore, it must be accounted for, as well. The oscilloscope voltage is

$$\tilde{V}_0(j\omega) = \tilde{H}_c(j\omega)\ \tilde{V}_1(j\omega)$$

$$= \tilde{H}_c(j\omega)\ \tilde{H}(j\omega)\ \tilde{I}_z(Z,j\omega),$$

where $\tilde{H}_c$ denotes the cable transfer function. This transfer

function is constructed by accounting for the electrical length of the cable in the phase of H_c. The magnitude function is constructed by linearly interpolating the logarithmic representation (dB) of the manufacturer's attenuation data (Table 1) for the cable. Thus, the product $\tilde{H}_c(j\omega)\,\tilde{H}(j\omega)$ is, in practice, deconvolved from a measured waveform to recover $I_z(Z,t)$.

Table 1. Attenuation of Coaxial Cable

Manufacturer: Uniform Tubes, Inc.

Micro-Coax Part No.: UT - 20

Typical Attenuation (dB/100')

0.5 GHz	1.0 GHz	5.0 GHz	10.0 GHz	20.0 GHz
51.0	72.0	163.0	233.0	334.0

The electrical parameters of our loop are calculated using the formulas developed above and the dimensional parameters summarized in Table 2. The electrical parameter results are summarized there, as well. The shape parameter $\Omega = 2\ln(\pi W/a)$ takes on a value of 7.341 in this case. This value represents a relatively "fat" loop and is near the limit of applicability of the Whiteside theory. The current in the circuit shown in Figure 7 is seen to be proportional to the magnetic field through the loop. The parameters L and $\tilde{Z}_1$ complete the circuit description.

Table 2. Loop Parameters (Present Work)

W	0.125 inch	$\tilde{I}$	$5.213\ 10^{-03}\ \tilde{H}_n^i$
a	0.115 inch	L	3.817 nH
Ω	7.341	$\tilde{Z}_1$	50 ohm

2.4 Calibration Jig

A probe must be calibrated in order to determine the true response of the transient signal. A rigid, 45 cm long, coaxial transmission line was used to calibrate probes in this work. The center conductor is 3/8 inch O.D. hollow brass tubing with an 0.075 inch slot. The outer conductor is 0.785 inch I.D. copper tubing. The outer conductor is actually that of EIA Standard 7/8 inch rigid airline, while the center conductor is slightly larger. The center conductor was chosen such that it has the same curvature as the scatterer of interest. The result of the combination is that the characteristic impedance of the coaxial jig is 44.33 ohms, the capacitance per meter is 75.2 Picofarads, and the inductance per meter is 0.148 Microhenrys. Figure 8 shows a photograph and line drawing of the jig, along with an adaptor between 7/8 EIA and Type-N connectors.

Because of the center conductor size chosen, a mismatch results between a 50 ohm Type-N cable feeding the jig and the 44.33 ohms of the jig. In addition, the adaptor potentially introduces a local junction reactance. The two effects are represented schematically in Figure 8c. This mismatch is conceivably frequency-dependent, thus introducing the possibility of waveform distortion to a transient excitation.

The frequency dependence of the junction is accounted for in terms of a transmission coefficient

$$\tau_{10} = \tilde{V}_1/\tilde{V}_0 \ ,$$

where $\tilde{V}_1$ is the forward-going wave on the jig transmission line and

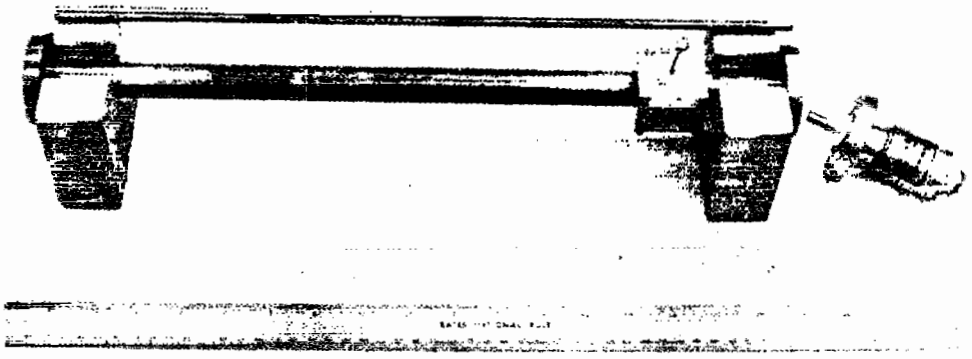

(a)

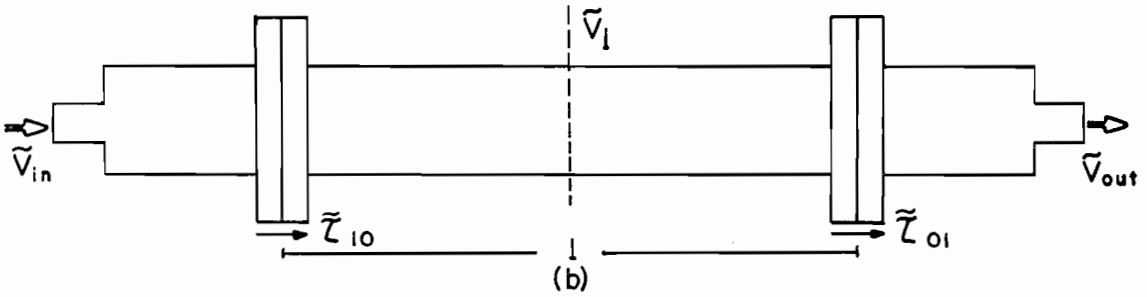

(b)

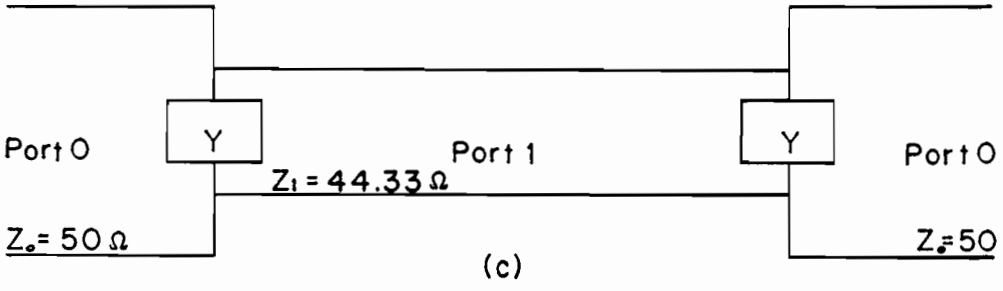

(c)

Figure 8. (a) Photograph of a coaxial jig and a 7/8" to N adaptor used for measurement of known fields.

(b) 7/8" rigid coaxial transmission line and 7/8" to N adaptors used to calibrate the current probe.

(c) Approximate junction representation between adaptor and transmission line.

$\tilde{V}_0$ is the incident wave on the 50 ohm line. This coefficient cannot be measured directly because of the difficulty associated with measuring a voltage on the 44.33 ohm line. The following indirect method was used instead.

A measurement is made through the jig using two identical Type-N to EIA 7/8 inch adaptors. The voltages $V_{in}(t)$ and $V_{out}(t)$, whose transforms are shown in Figure 8b, are measured.* They are both defined on 50 ohm cables, so this measurement is straightforward. The adaptors are presumed to be identical so that the symmetric transmission line model shown in Figure 8c is valid. From the model we determine that

$$\tilde{V}_{out} = \tilde{V}_{in}\, \tau_{10}\, \tau_{01} e^{-j\omega l/c} \qquad (2)$$

where

$$\tau_{10} = 2Z_1/(Z_1 + Z_0 Z_1 Y + Z_0)$$

and

$$\tau_{01} = 2Z_0/(Z_1 + Z_0 Z_1 Y + Z_0) \ .$$

The effect of multiple reflections in the jig region is not expressed in (2). In the measurement, the observations of $V_{out}(t)$ and $V_{in}(t)$

---

*Transform data are computed numerically from a 512 sample digitized record of a 5 nanosecond duration waveform. Only every 32nd point of data is necessary to satisfy the Nyquist criterion for the significant spectrum of the pulse generator. Therefore, the transforms displayed herein were computed as the average of 32 phase adjusted transforms of subsequences of the data record. Each subsequence is filled with trailing zeros to a length of 256 in order to maintain good frequency resolution.

are conducted over a time window of 2-1/2 nanoseconds so that multiple reflection effects are time-gated out of the observation. Thus (2) is the correct model of the observed voltage $\tilde{V}_{out}$ in the Fourier transform domain.

We wish to identify τ_{10} in (2) from observation of $\tilde{V}_{out}/\tilde{V}_{in}$. We observe that

$$\tau_{10} = Z_1\sqrt{\tau_{10}\tau_{01}/Z_0Z_1}\ , \qquad (3)$$

and that

$$\tau_{01}\tau_{10} = e^{-j\omega l/c}\ \tilde{V}_{out}/\tilde{V}_{in} \qquad (4)$$

Thus, time-gated transient observation of $V_{in}(t)$ and $V_{out}(t)$, followed by numerically Fourier transforming them, allows computation of (4). Since Z_0 and Z_1 are known, the desired transmission coefficient can be computed from (3).

The method described above was implemented using an IKOR "IMP" generator as a transient signal source and a Tektronix P7001 Oscilloscope* with a 7S12/S-6/S-53 sampling scope configuration. The input waveform $V_{in}(t)$ and its spectrum are shown in Figure 9. The bandwidth of the IMP generator waveform allows determination of the transmission coefficient to near 2 GHz. The result is shown in Figure 10. It is seen that the coefficient is flat with frequency and that the impedance ratio $Z_1/\sqrt{Z_0Z_1}$ in (3) (0.94 in the

*The P7001 is a digitizing oscilloscope and is interfaced to a Tektronix 4051 desktop computer. In this measurement, all waveforms used result from the averaging of 16 individual waveform observations acquired by the 4051. This procedure was used consistently in all measurements reported in this work, unless otherwise stated.

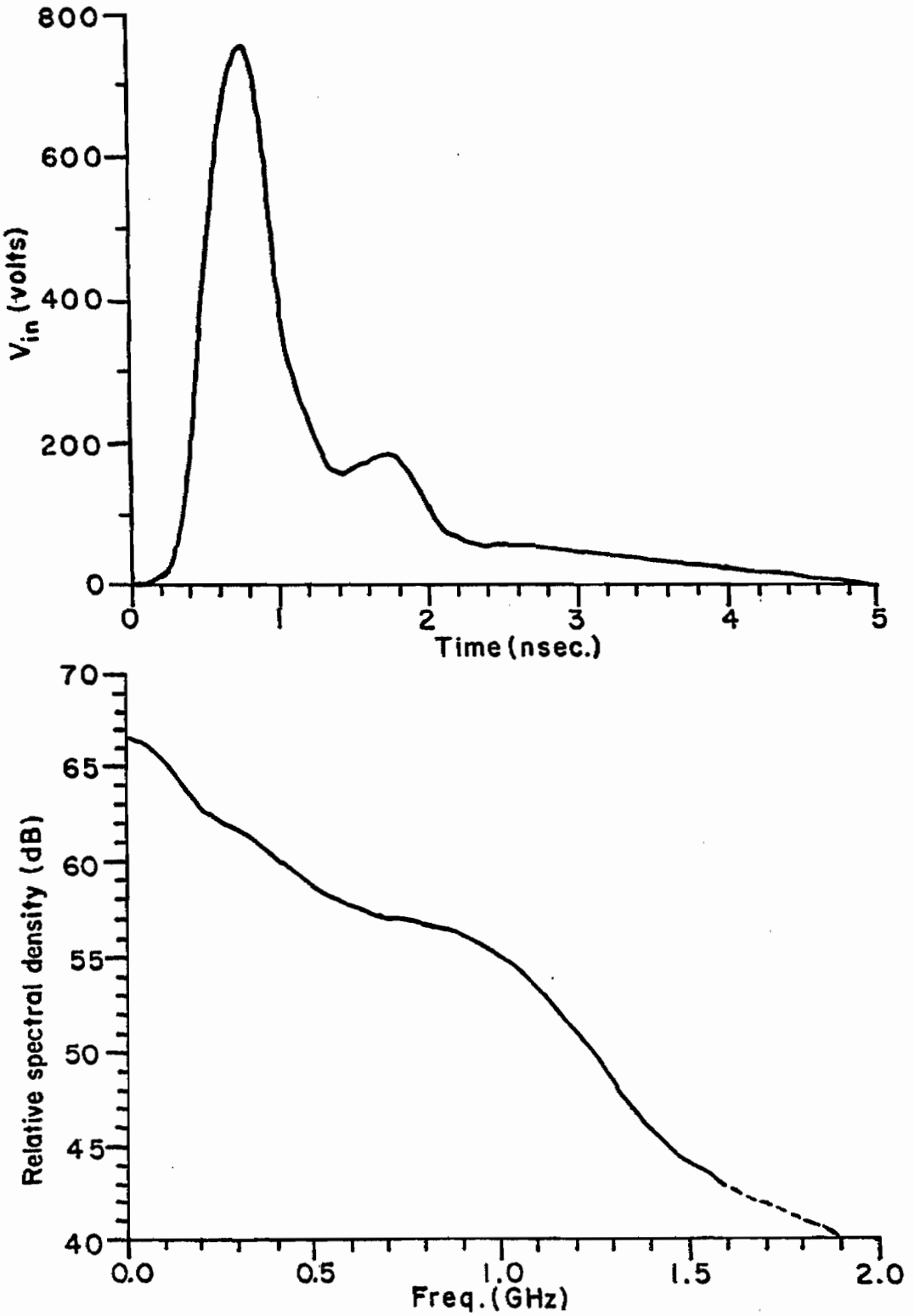

Figure 9. Average of 16 waveforms produced by the pulse generator used in this experiment and its spectrum.

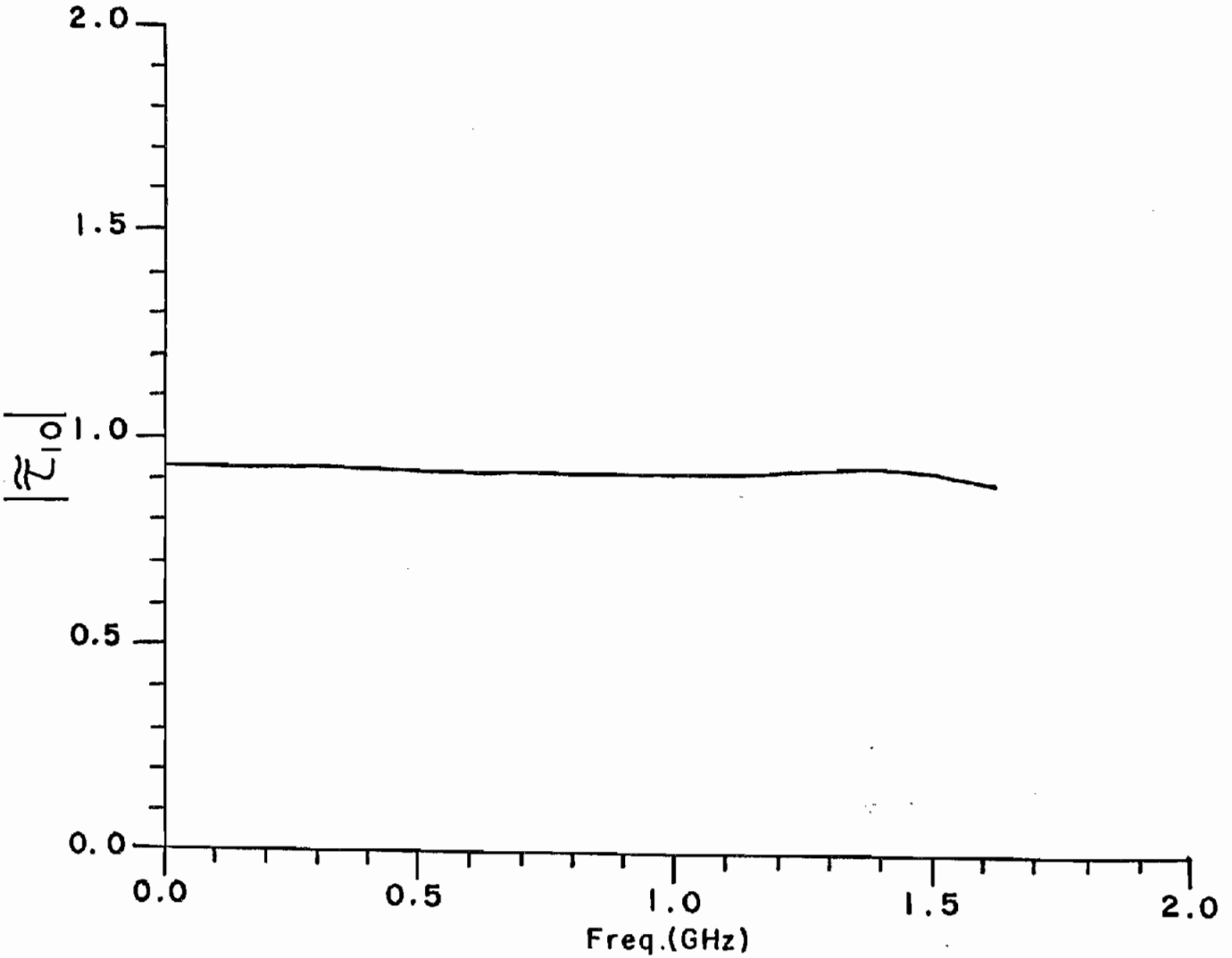

Figure 10. Transfer function of the transition of Type-N connector to 7/8" coaxial line.

present case) fully accounts for it.

2.5 Transfer Function of Cable Adaptors

An OSM to N adaptor had to be employed in order to measure the $\tilde{V}_{in}$ and $\tilde{V}_{out}$ using the Tektronix Sampling Heads. This adaptor cannot be ignored in the calibration procedure and, therefore, its transfer function was determined in the following fashion. Three different Type-N to OSM adaptors were used in the measurement:

N-female to OSM-female;

N-male to OSM-male;

N-female to OSM-male.

The combination of these adaptors is shown in Figure 11. The three adaptors are presumed to have identical transfer functions. This is, of course, an approximation. It is reasonable except for small differences in electrical length, and these differences are smaller than the time resolution of the instrumentation.

Subject to this assumption, the spectra of the voltage waveforms $\tilde{V}_2$ and $\tilde{V}_3$ (Figure 11) can be written as follows:

$$\tilde{V}_2 = \tilde{H}_3 \, \tilde{H}_2 \, \tilde{V}_g$$

and

$$\tilde{V}_3 = \tilde{H}_3 \, \tilde{H}_2 \, [\tilde{H}_2]^2 \, \tilde{V}_g$$

where $\tilde{H}_3$ is the transfer function of the attenuators, $\tilde{H}_2$ is the transfer function of the N to OSM adaptor, and $\tilde{V}_g$ is the generator waveform. $\tilde{H}_2$ can be found, from dividing the above equations, to be

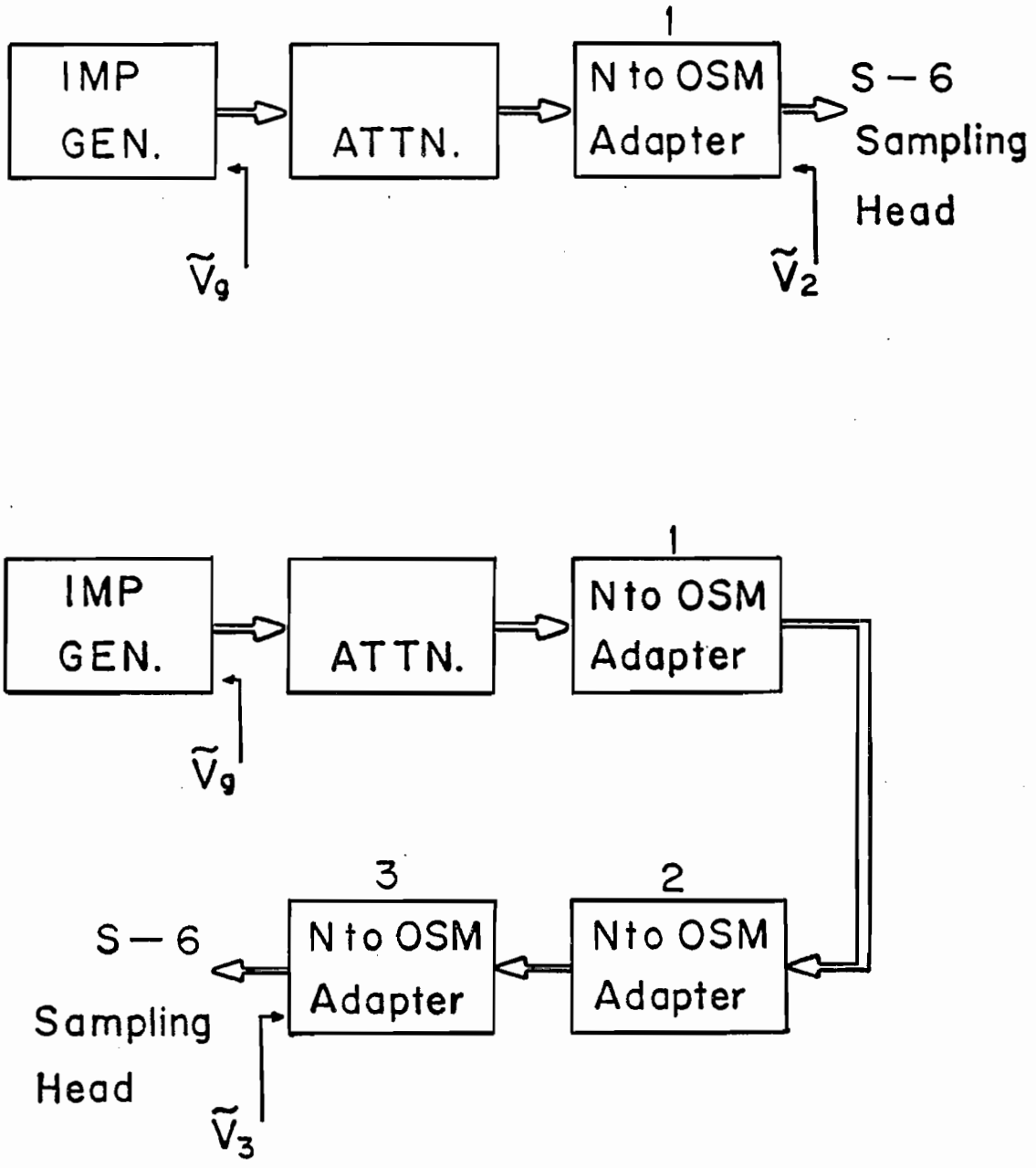

Figure 11. Block diagram to compute transfer function of N to OSM adaptor by measuring V_2 and V_3.

1: N-female to OSM-male;
2: N-female to OSM-female;
3: N-male to OSM-male.

$$\tilde{H}_2 = \sqrt{\tilde{V}_3/\tilde{V}_2} \quad .$$

2.6 Probe Transfer Function

The preceding two sections provide the basis for measuring the frequency response of the loop probes. The measurement configuration is shown in Figure 12a. The slot of the center conductor is taped with conducting tape to eliminate coupling to the coaxial region formed by the center conductor and the probe push rod. The input voltage spectrum $\tilde{V}_{in}$ is determined by measuring $V_{in}(t)$ through known attenuation and an N-female to OSM male adaptor. The effect of the intervening components is subsequently deconvolved from the spectrum of $V_{in}(t)$. The probe response spectrum is determined from $V_p(t)$, which can be measured directly. A specimen of the latter waveform is given in Figure 12b. That it is roughly the time derivative of $V_{in}(t)$ is observable through comparison with Figure 9. The waveform is gated out after 2.5 nanoseconds to eliminate the reflection from the other end of the calibration jig. The probe transfer function is defined as the probe response voltage spectrum divided by the spectrum of the net current flowing on the center conductor of the calibration jig. In terms of measurable quantities,

$$\begin{aligned} \tilde{H}_p(j\omega) &= \tilde{V}_p(j\omega)/\tilde{I}(j\omega,d) \\ &= \tilde{V}_p Z_1/(\tau_{10}\tilde{V}_{in}e^{-j\omega d/c}) \quad . \end{aligned}$$

Figure 13 shows the amplitude of the transfer function of the probe. The solid line and the dashed line are the observed transfer functions of two different probes computed using the measured waveforms.

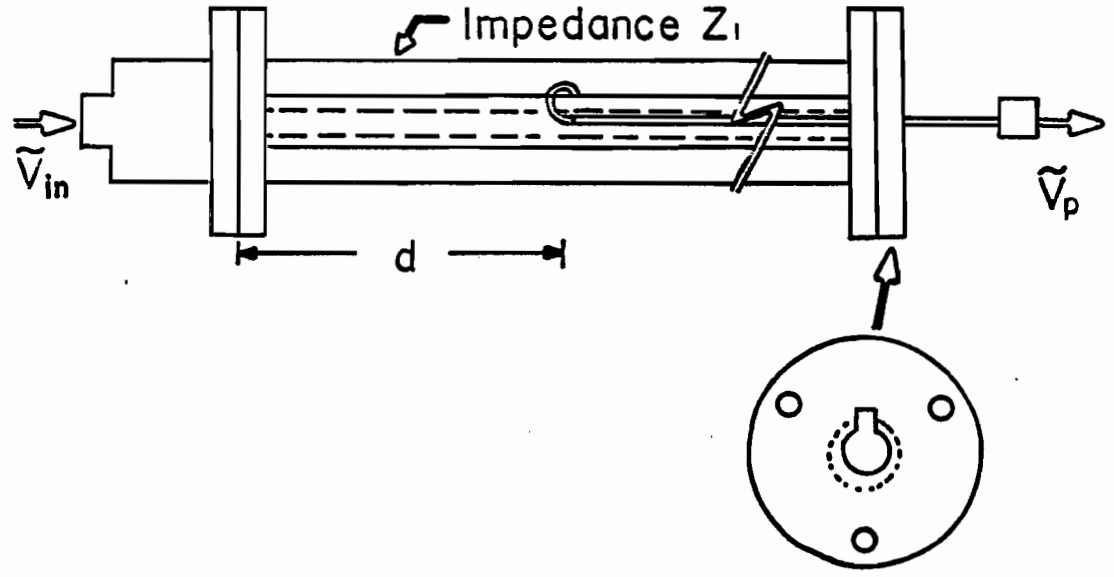

(a)

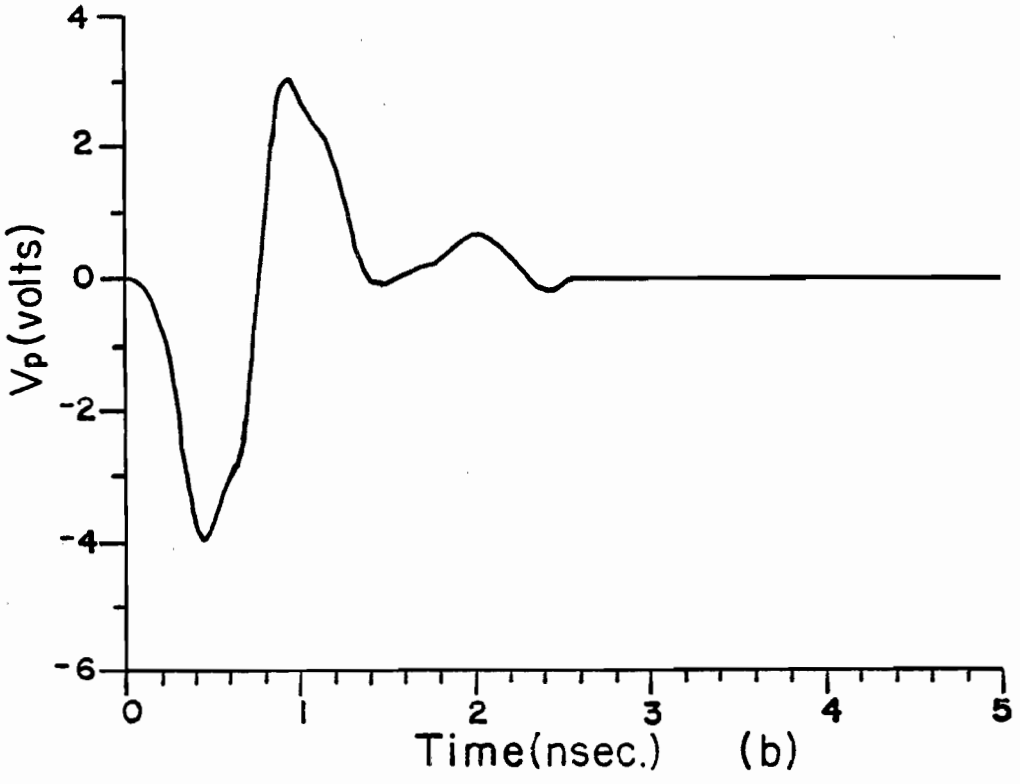

Figure 12. (a) Cross-section of the calibration jig used to calibrate the probe.

(b) A probe output $V_p(t)$ sampled by a current probe where the source of excitation is the pulse shown in Figure 9.

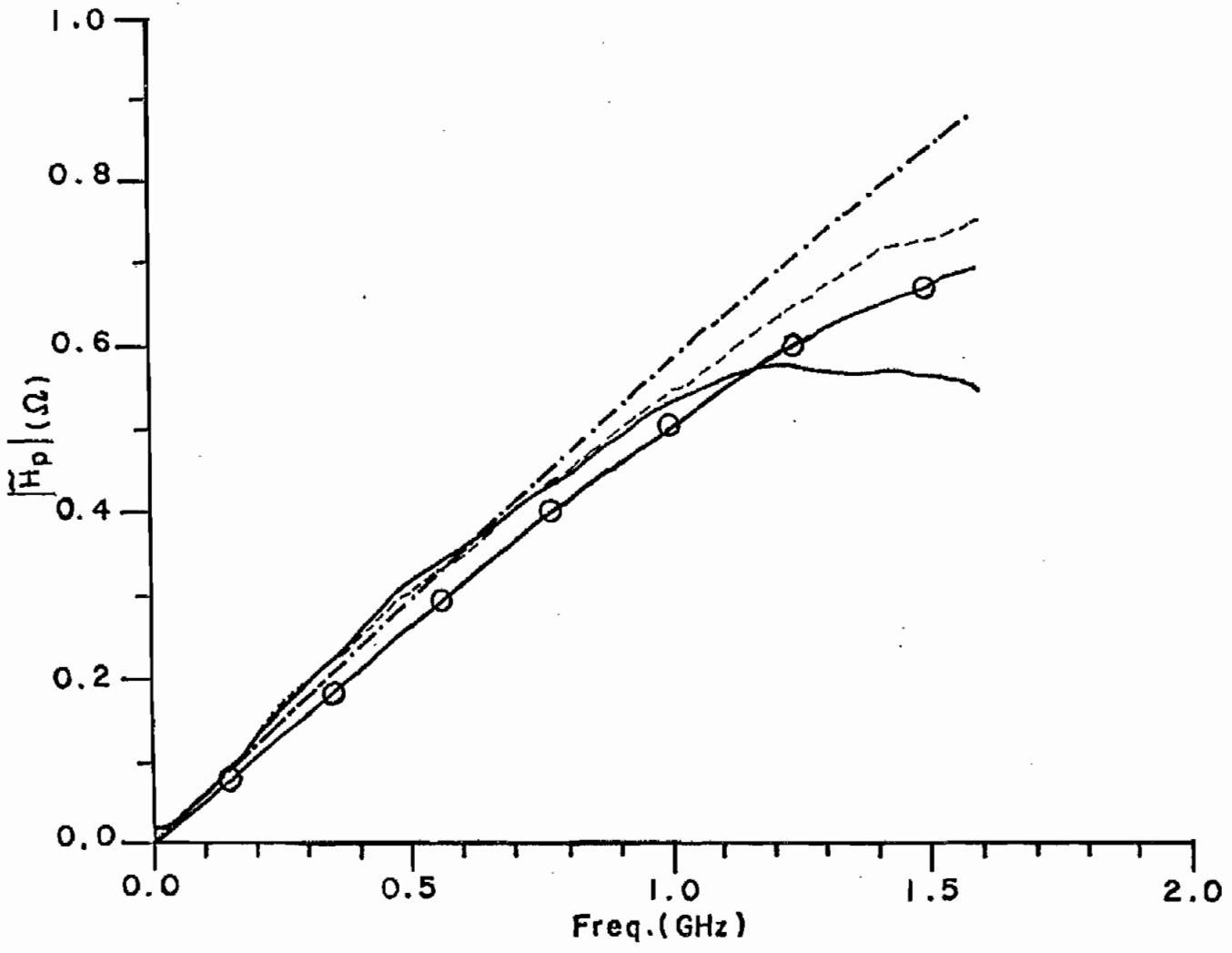

Figure 13. Experimental and theoretical transfer functions obtained for 0.125" probes. (a) theoretical from equivalent circuit - dot-dashed; (b) theoretic with cable attenuation included - solid/ circles; (c) experimental Probe no. 1 - dashed; (d) experimental Probe no. 2 - solid.

The dot-dashed line is the result of the derivation presented in section 2.3. As we pointed out earlier, the 0.023 inch cable has an attenuation which is significant at higher frequencies in the spectrum. The curve marked with circles is the result of the adjusting of the theoretical (dot-dashed) curve to include attenuation effects. It is seen that the measured responses of both probes are underestimated by the attenuation-corrected theoretical result at lower frequencies. In fact, even the theoretical transfer function, which does not include attenuation, lies below the measured response curve. The theoretical results are based on the nominal 0.125 inch diameter of the loops. It is possible that the actual diameters are somewhat larger.

The general trends in the measured curves indicate the proper effects of attenuation. Since the attenuation model used is based on bounding data supplied by the manufacturer, it is likely that the attenuation-corrected theoretical result is somewhat too low.

Up to roughly 1 GHz, the two probes show comparable response features. The particular source of disagreement above 1 GHz is not readily apparent. It must be associated with some feature differing between the two fabrications, but the identity of the particular feature has not been uncovered.

A smooth sinusoidal component is observed to be superimposed on the measured transfer function. A similar component is seen in the spectrum of the input pulse. This may be present for the following reason. The IKOR IMP pulse generator uses a spark-gap switch in generating the waveform. This type of generator fails to produce identical pulses shot-to-shot. The Digitizing

Oscilloscope takes the average of the waveform point by point in the sampling process, based on a different excitation pulse each time. Because of the rapidity of the events being measured, it is not possible to circumvent the sampling process, of course.

The phase information associated with Figure 13 was not extracted or used explicitly. The various adaptors required in calibrating a phase (time) reference for the jig preclude doing so in any accurate fashion. In practice, the measured data waveforms are all time referenced, based on a causality criterion.

III. IMPLEMENTATION OF PROBING SCHEME ON A CYLINDRICAL SCATTERER

3.1 Introduction

The net axial surface current on a thin cylindrical scatterer was measured using the probing method. The currents were induced by the electromagnetic field radiated by a transmitting antenna nearby. The Singularity Expansion Method description of the cylinder was extracted from this set of data and compared with Tesche's computed results [31].

A thin cylinder was chosen for the following reasons. The thin cylinder has rotational symmetry and the radius is small compared with the length; therefore, one dimensional analysis of the current on it is sufficient. The probe carriage is fitted inside the scatterer into a longitudinal slot, thereby making it possible to locate the probe at any point along the structure. Thus, flexibility as to probing points is provided in evaluating the present probing method. A thin cylinder is relatively easy to solve theoretically, and reliable comparison data is readily available. We ultimately do SEM parameter extraction from the data and the thin cylinder SEM description is reliably characterized.

3.2 Measurement Configuration

A detailed description of the transient measurement system is presented in this section.

A block diagram of the measurement facility is sketched in Figure 14 along with a photograph of the inside of the facility.

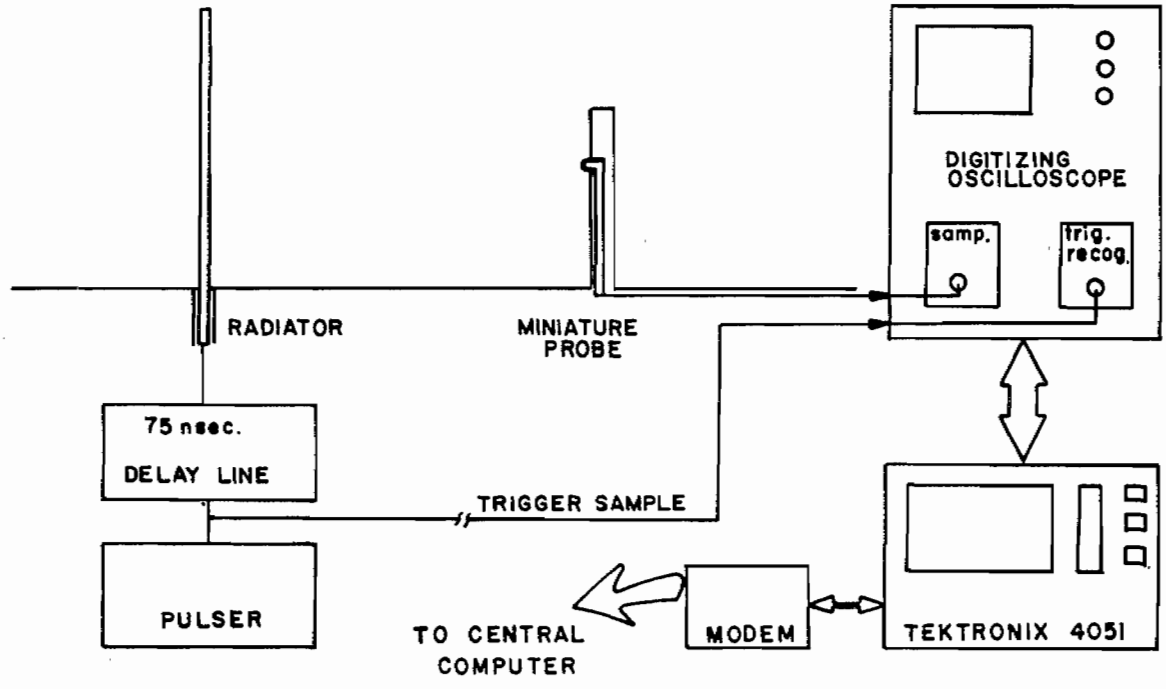

(a)

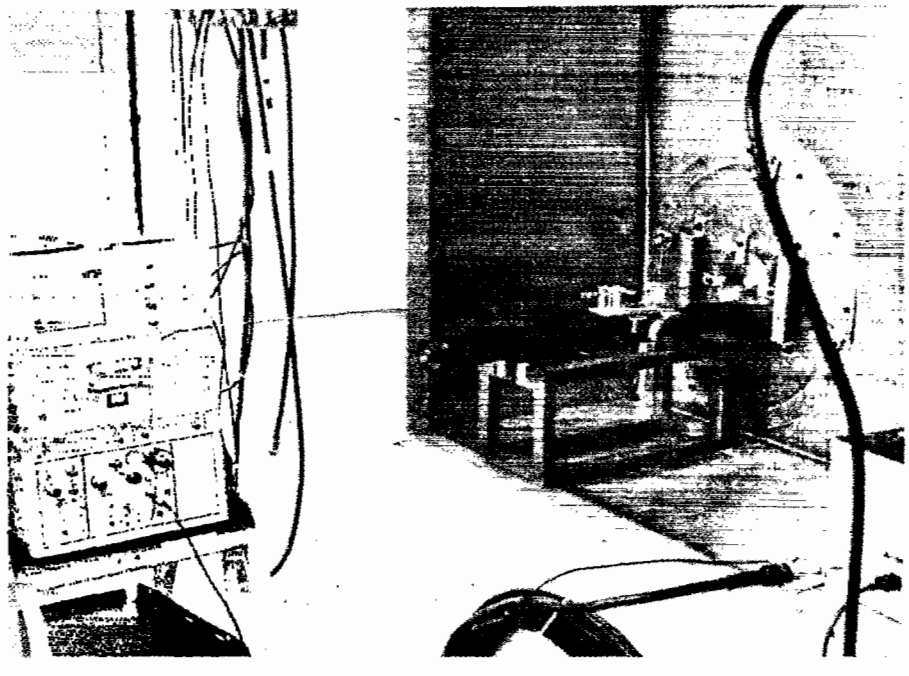

(b)

Figure 14. (a) Block diagram of transient antenna range facility.

(b) The measurement facility photographed from behind the ground plane.

The scatterer is formed from brass tubing 30.0 cm long and 3/8 inch in outer diameter. It carries a longitudinal slot of width 0.075 inch. A close up of this scatterer is pictured in Figure 15. The slot of the scatterer is taped with conducting tape with the probe in place. It is mounted on a brass disk so that it can be installed readily into the ground plane. The location of the probe can be determined using the scale on the positioning apparatus shown in Figure 16a. This carriage is mounted behind the disk where the scatterer is attached. The pushrod for the probe is attached to a calibrated stop on the movable arm of the probe carriage. Figure 16b pictures the scatterer's mounting disk from the back side of the ground plane with probe-positioning jig in place. The probe is oriented such that the plane of the probe is perpendicular to the direction of propagation from the transmitting antenna.

The transmitting antenna is a long cylinder made of brass tubing. It is 1.71 meters long and 0.25 inches in diameter at the base. The radius is stepped down to smaller sizes of brass tubing away from the ground plane to reduce the weight, and thereby droop, since it is a horizontally-mounted structure. The transmitting antenna and the scatterer are mounted at the center portion of a 20 x 18 foot ground plane and they are 79 cm apart. Figure 17 shows the outside view of the ground plane. The circles in the center panel are the locations for the transmitting antenna and the scatterer model, respectively.

3.3 Instrumentation

A Digital Processing Oscilloscope (DPO) is used to sample the

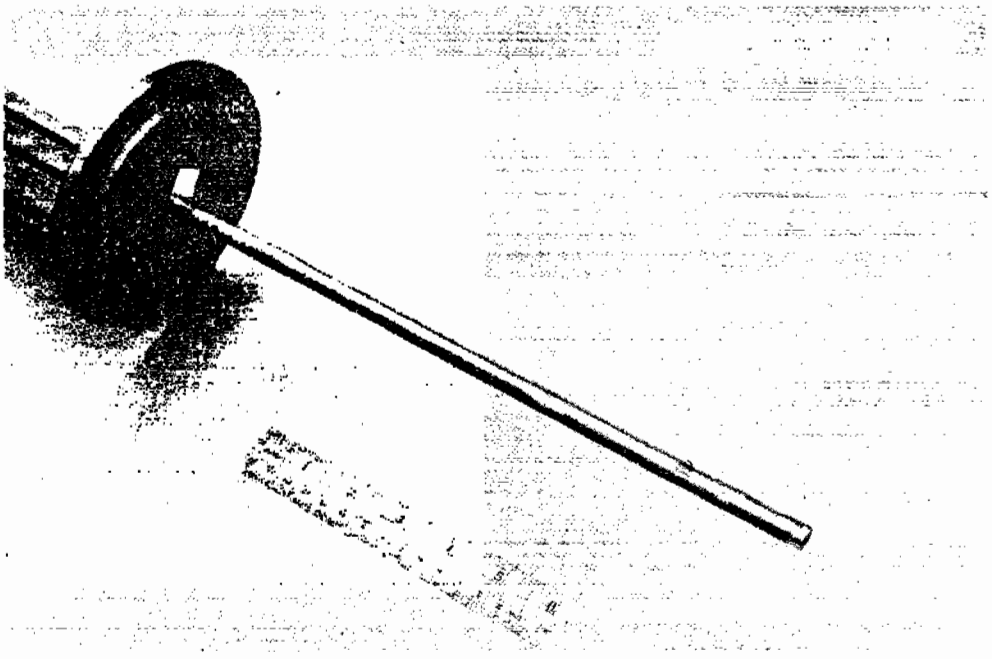

Figure 15. A close-up of a scatterer mounted on a brass disk. Probe is placed and the slot is taped with conducting tape.

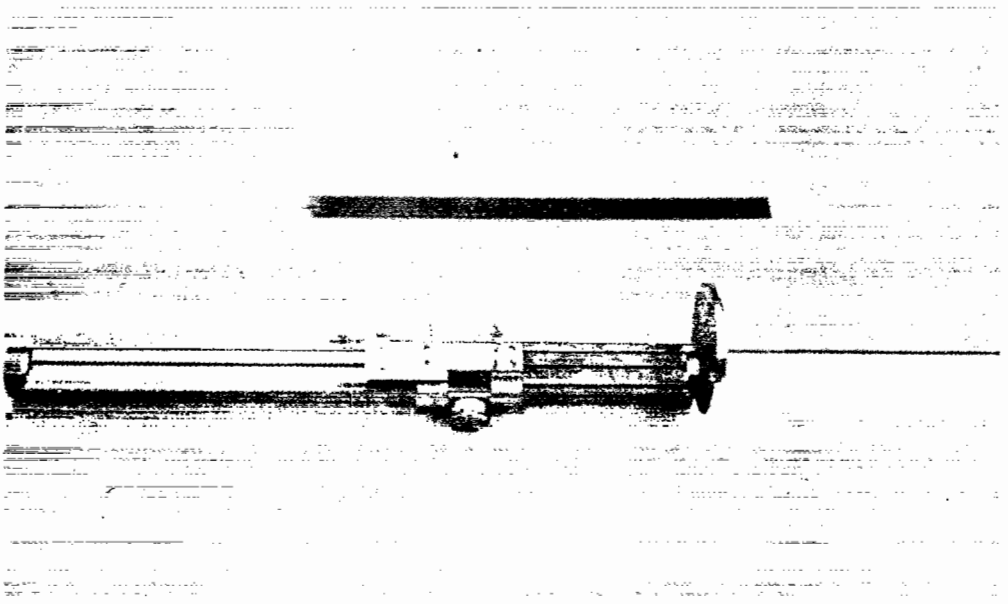

(a)

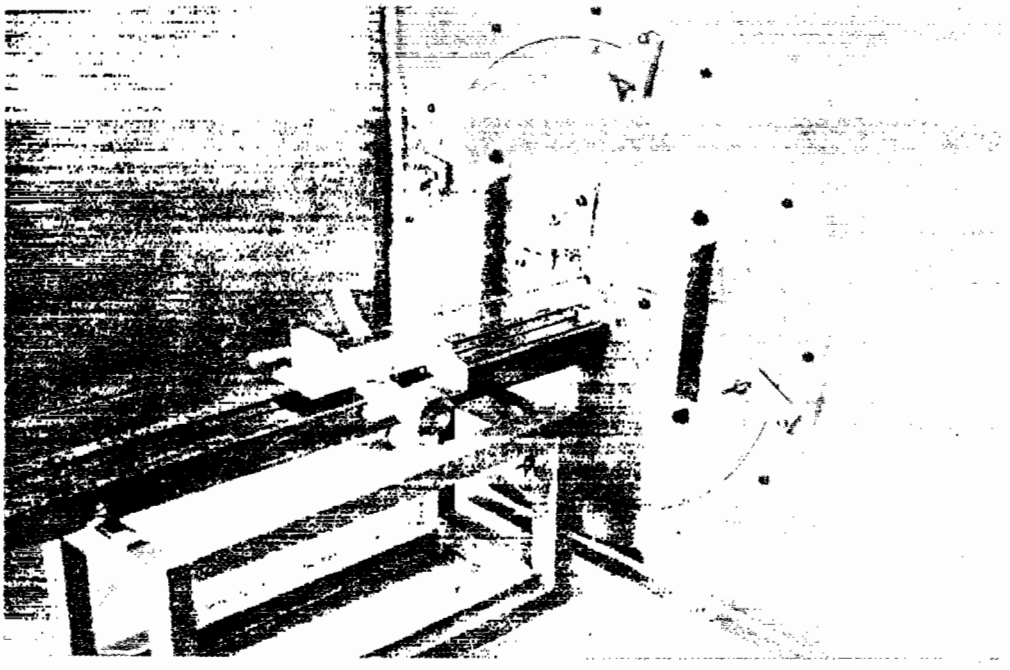

(b)

Figure 16. (a) A probe carriage is attached behind the disk where the scatterer is mounted.

(b) The probe carriage and disk mounted in the ground plane.

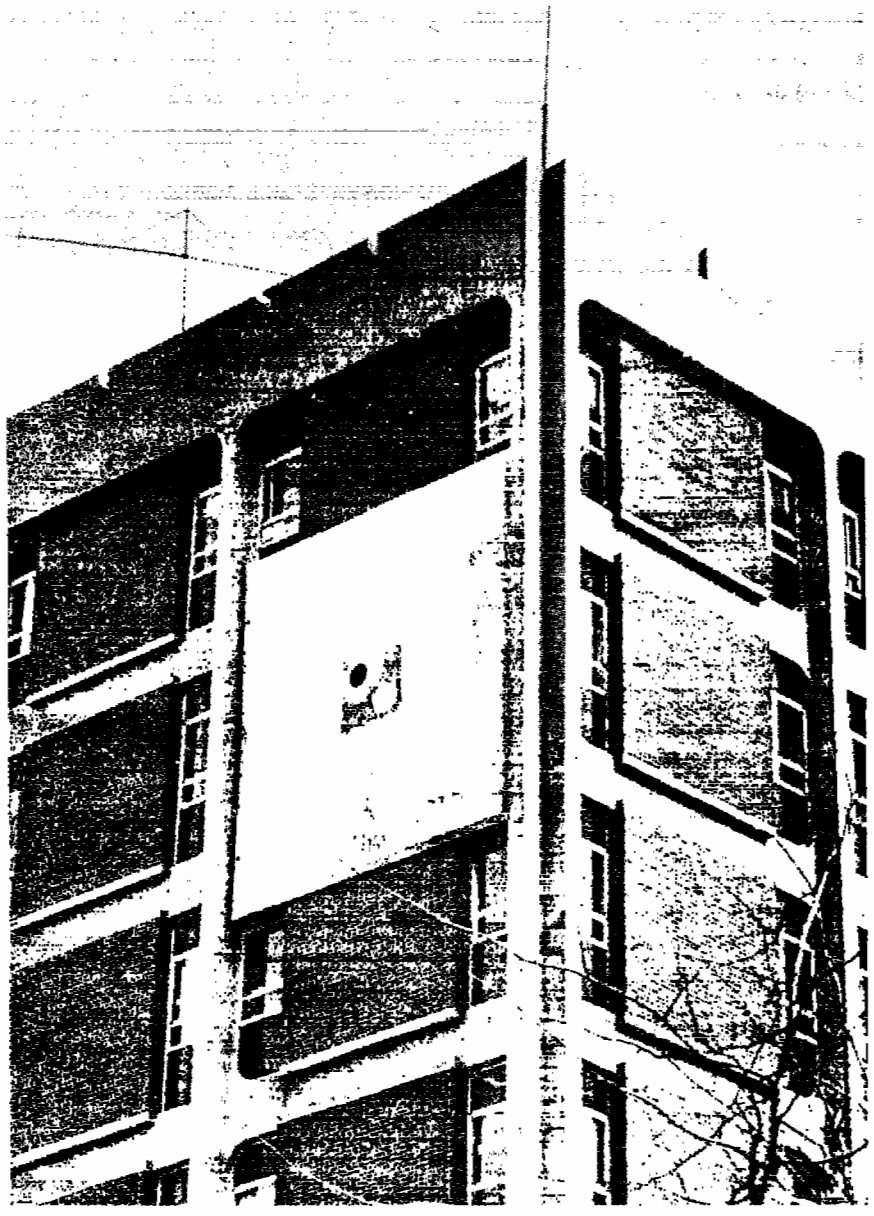

Figure 17. Ground plane for transient antenna system. The size of this ground plane is 18' x 20'.

waveform. The configuration of the DPO system includes a Tektronix D7704 Display Unit, P7001 Processor, 7S12 Sampler, S-6 Sampling Head, and S-53 Trigger Recognizer. The excitation source is an IKOR IMP generator whose waveform is shown in Figure 9 . A Tektronix 4051 desktop computer is used as a DPO controller and for intermediate data storage. All the data were shipped to the host computer, a DECSYSTEM-10, from the Tektronix 4051 for final numerical processing. The sampler requires a 75 nanosecond pretrigger pulse. Therefore, the excitation signal was passed through a 75 nanosecond delay line prior to delivery to the transmitting antenna. A 1.14-meter long and 0.141-inch diameter semirigid coaxial cable was used as an extension cable in connecting the probe and the S-6 Sampling Head.

3.4 Measured Data

Current waveforms were sampled at 19 locations along the scatterer for a time period of 5 nanoseconds. Sixteen waveforms were acquired and averaged as described in Section 2.4. The measured transfer function for the probe (as in Figure 13) was deconvolved from the measured waveform by taking a forward Fourier transform, dividing out the probe response, and inverse transforming. This deconvolution fails at zero frequency because the probe transfer function properly is zero there. Thus, the DC (zero frequency) level of the resulting waveforms is unreliable. This level can be corrected by the appropriate use of interpolation in the frequency domain. The DC level of the waveform has no bearing on the resonant modes derived in SEM extraction. Since the ultimate utility

of this work is in SEM extraction, this correction was not carried out here.

The result of these measurements and the subsequent reduction are given by the solid lines in Figures 18 through 36. The dot-dashed lines represent the results of direct integration of the measured waveforms. The dashed lines provide, for comparison, the result of a numerical model of the measurement configuration calculated with the TWTD transient scattering computer code from Lawrence Livermore Laboratories.*

The TWTD program was employed with some modification in order to incorporate the features of the spherical wavefront impinging on the scatterer in the experimental configuration. The radiated electric field used as the driving field in the TWTD program was computed using the results given by Harrison and King [35]. Their model was for an infinitely long cylindrical transmitting antenna. Our system is equivalent to their configuration since the response waveforms were gated off in time domain before the pulse radiated from the end of the finite-length antenna arrived at the scatterer. The input waveform in the Harrison and King model was taken to be the IKOR IMP generator waveform delivered to the transmitting antenna. The TWTD program is sensitive to noise present in the driving field data and it can be seen in late-time behavior of several of the Figures. The noise level is heavier when the

---

*TWTD is a computer code which computes the time history of the surface currents of a thin scatterer and details of the descriptions can be found in References [32], [33], and [34].

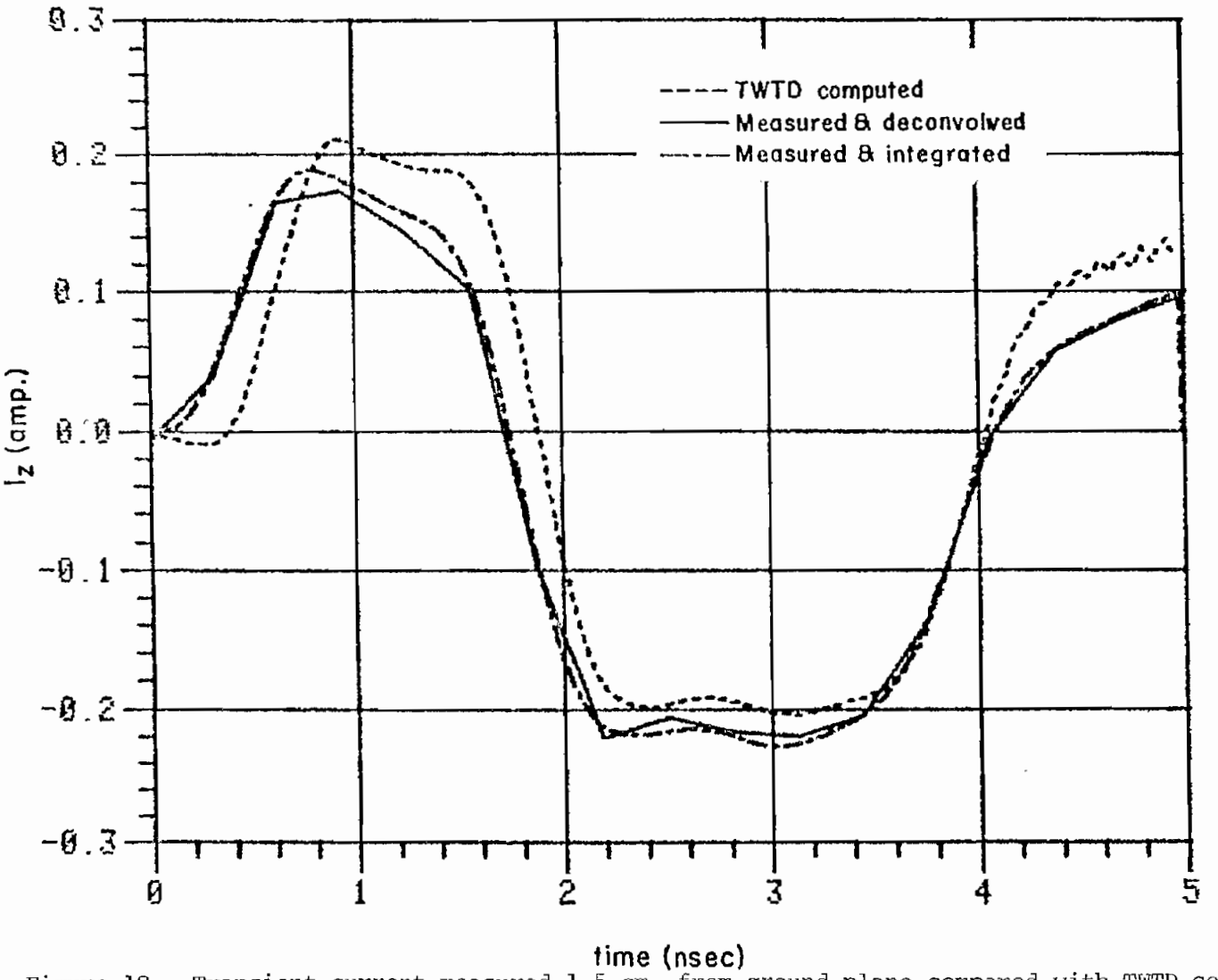

Figure 18: Transient current measured 1.5 cm. from ground plane compared with TWTD computation 1.3 cm. from ground plane.

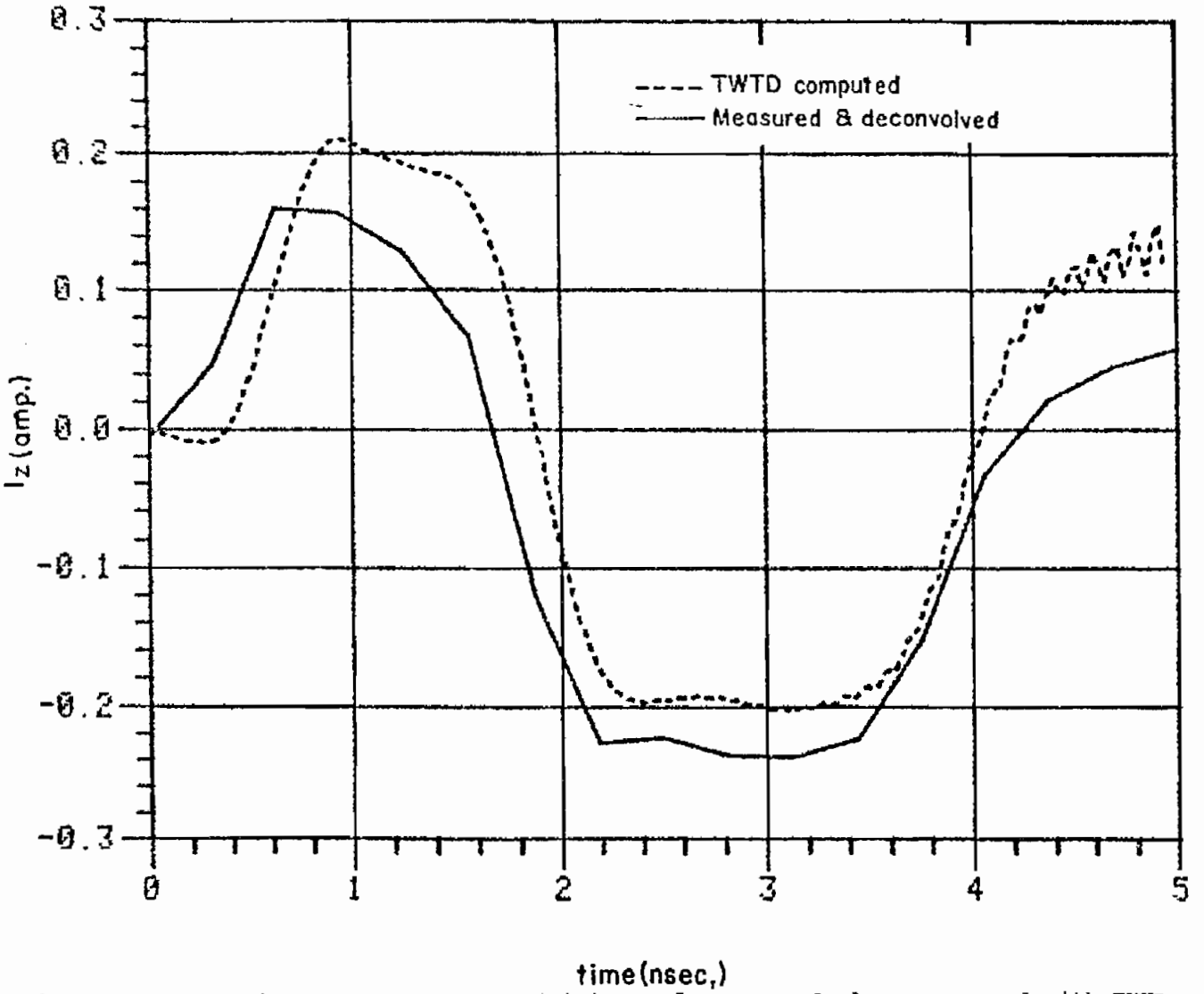

Figure 19. Transient current measured 3.0 cm. from ground plane compared with TWTD computation 3.0 cm. from ground plane.

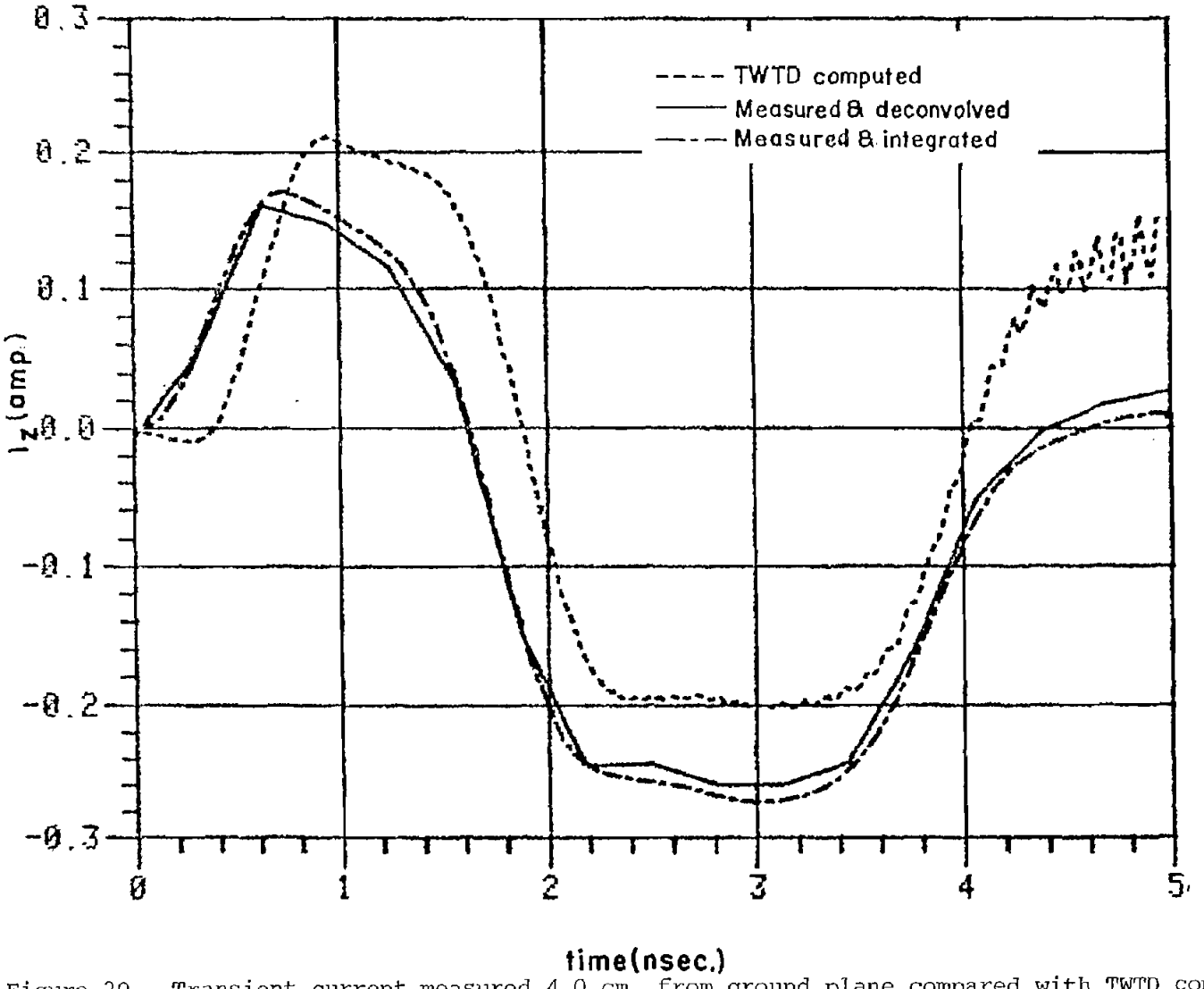

Figure 20. Transient current measured 4.0 cm. from ground plane compared with TWTD computation 3.9 cm. from ground plane.

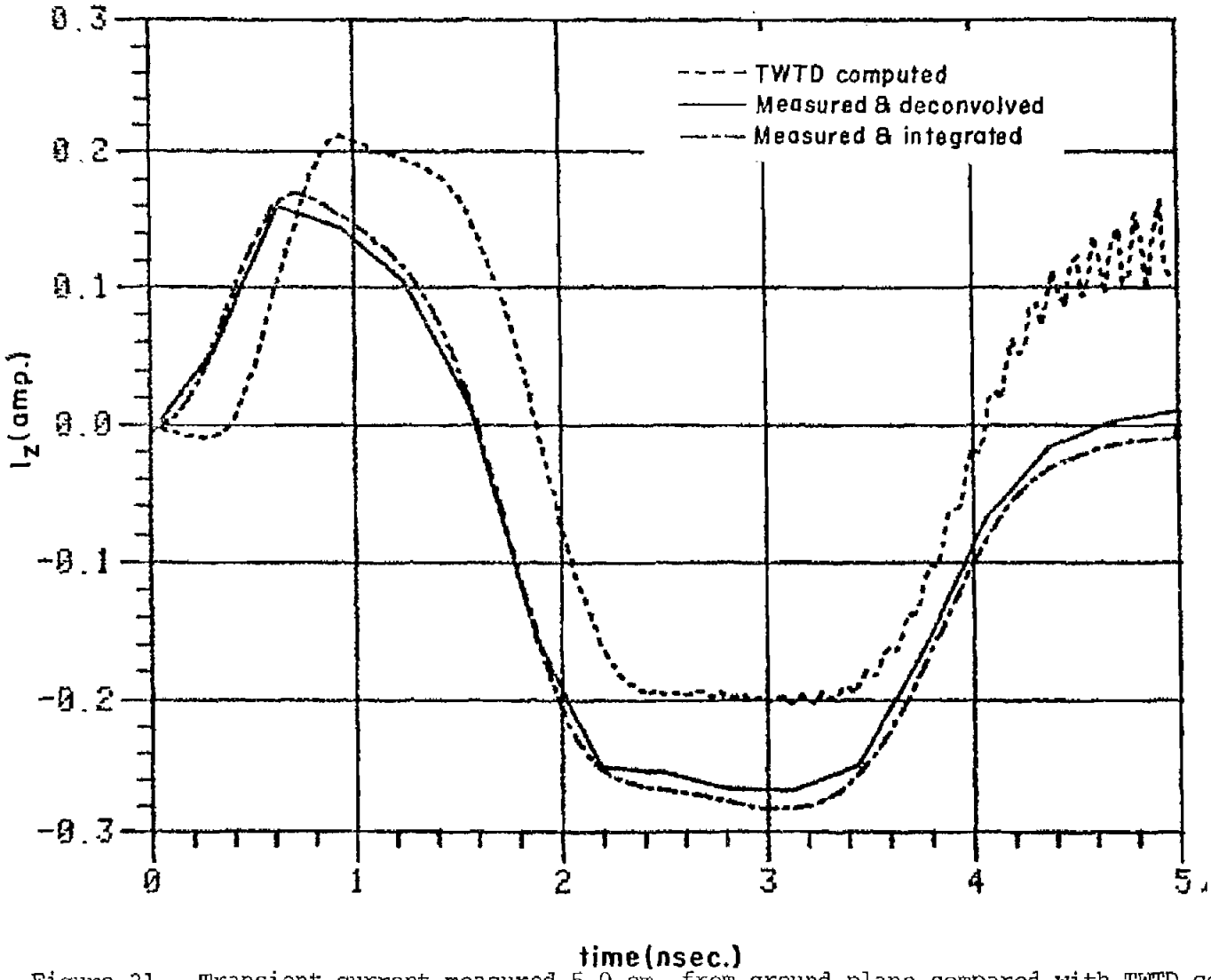

Figure 21. Transient current measured 5.0 cm. from ground plane compared with TWTD computation 4.7 cm. from ground plane.

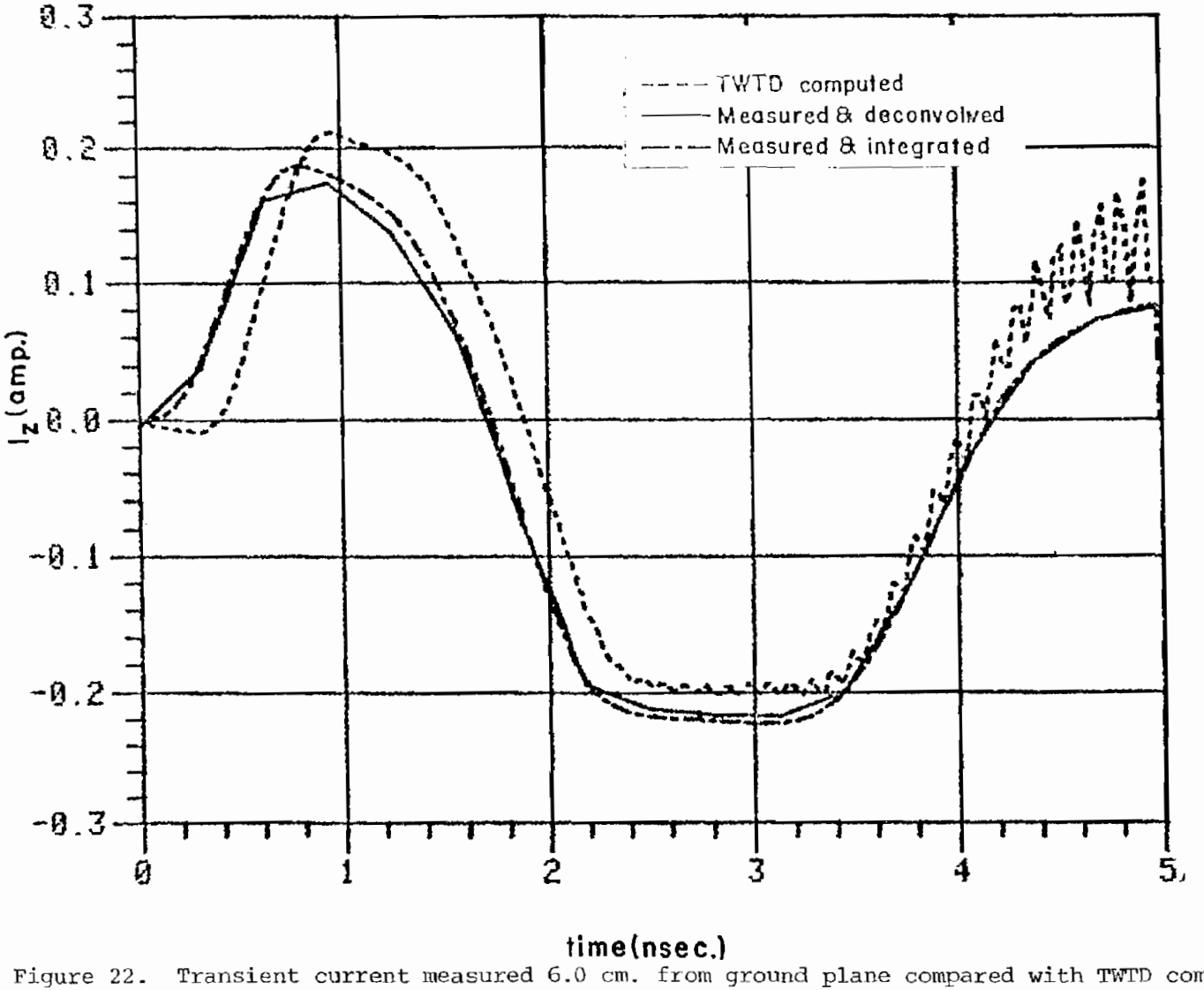

Figure 22. Transient current measured 6.0 cm. from ground plane compared with TWTD computation 6.4 cm. from ground plane.

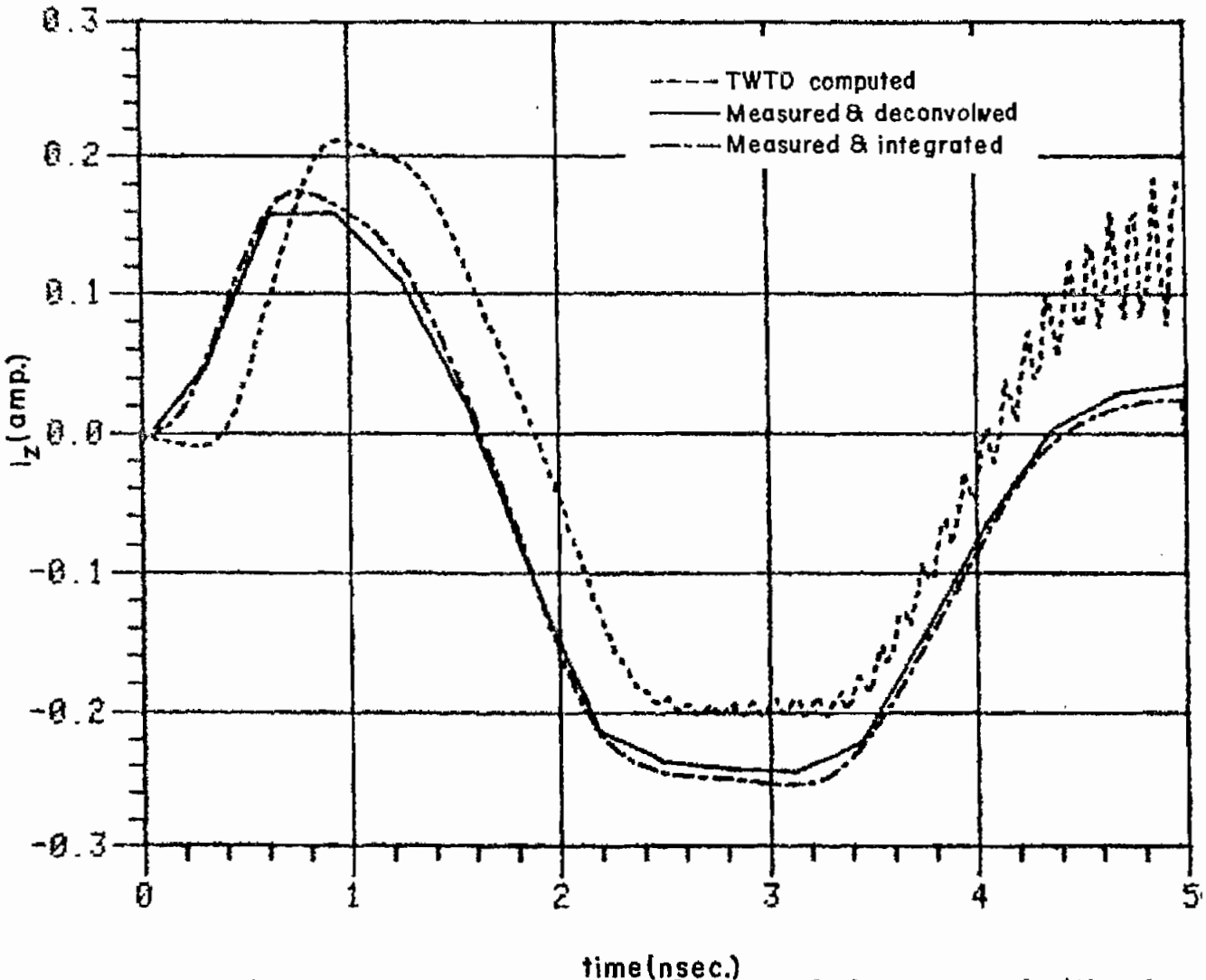

Figure 23. Transient current measured 7.0 cm. from ground plane compared with TWTD computation 7.3 cm. from ground plane.

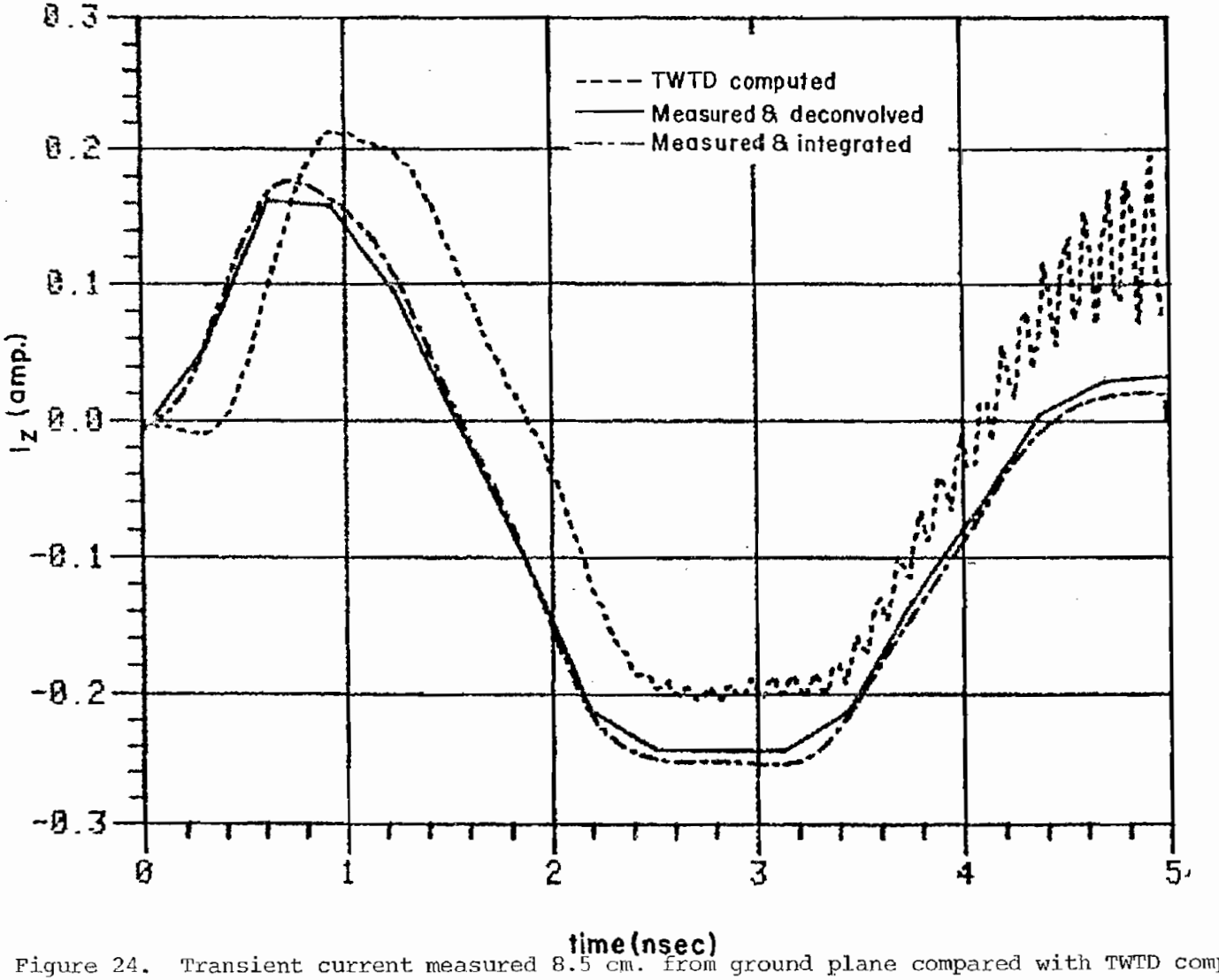

Figure 24. Transient current measured 8.5 cm. from ground plane compared with TWTD computation 8.1 cm. from ground plane.

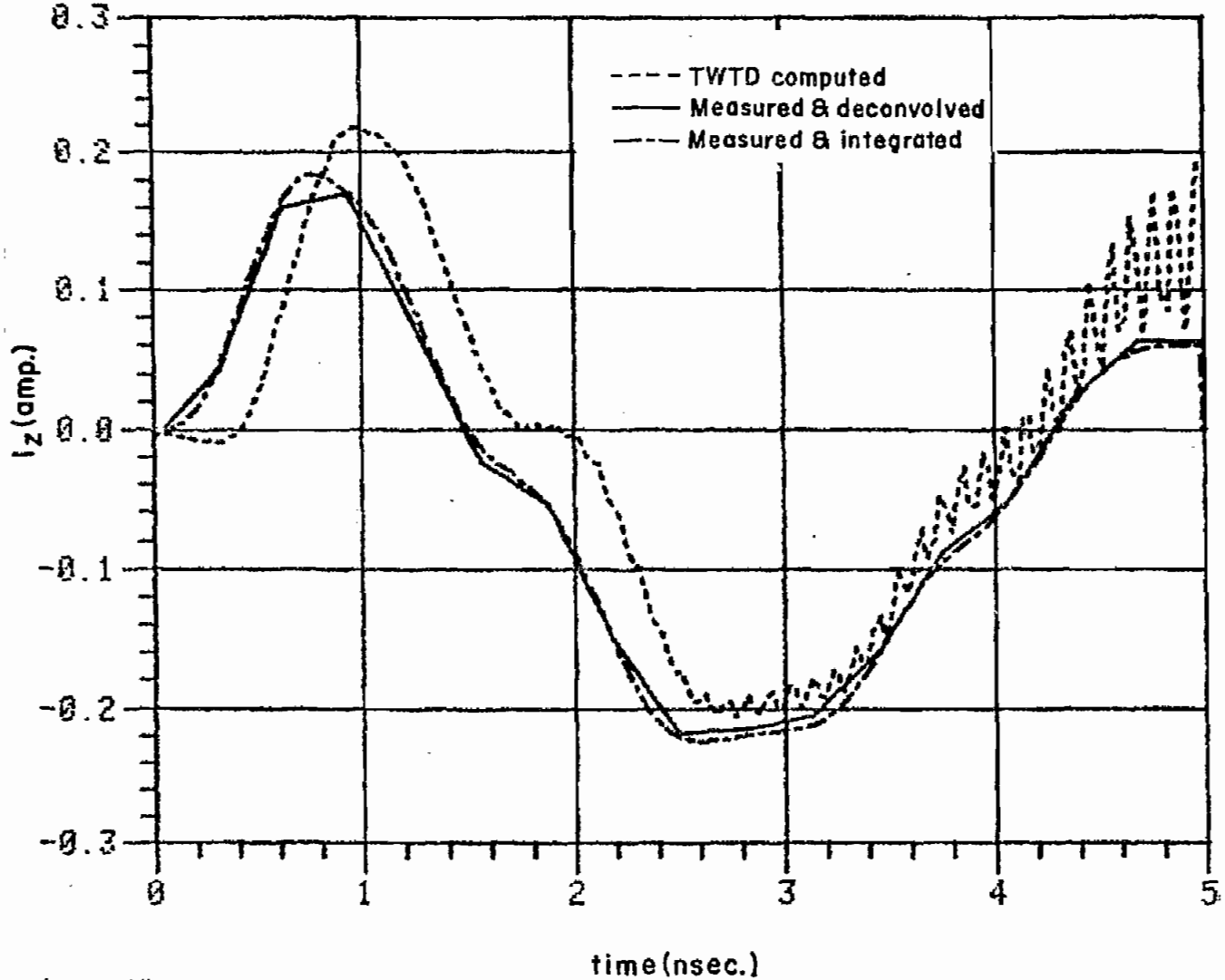

Figure 25. Transient current measured 11.0 cm. from ground plane compared with TWTD computation 10.7 cm. from ground plane.

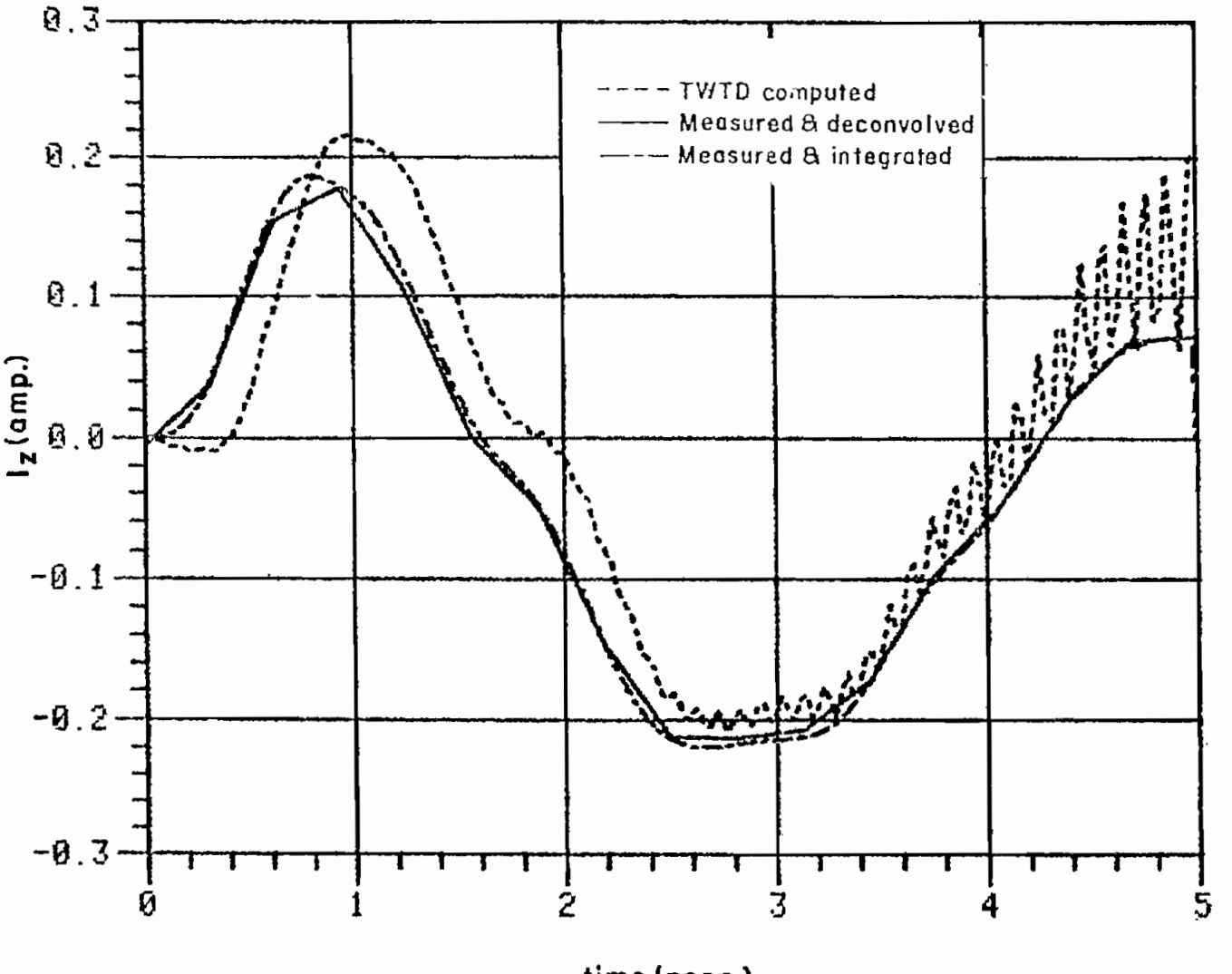

Figure 26. Transient current measured 12.0 cm. from ground plane compared with TWTD computation 12.4 cm. from ground plane.

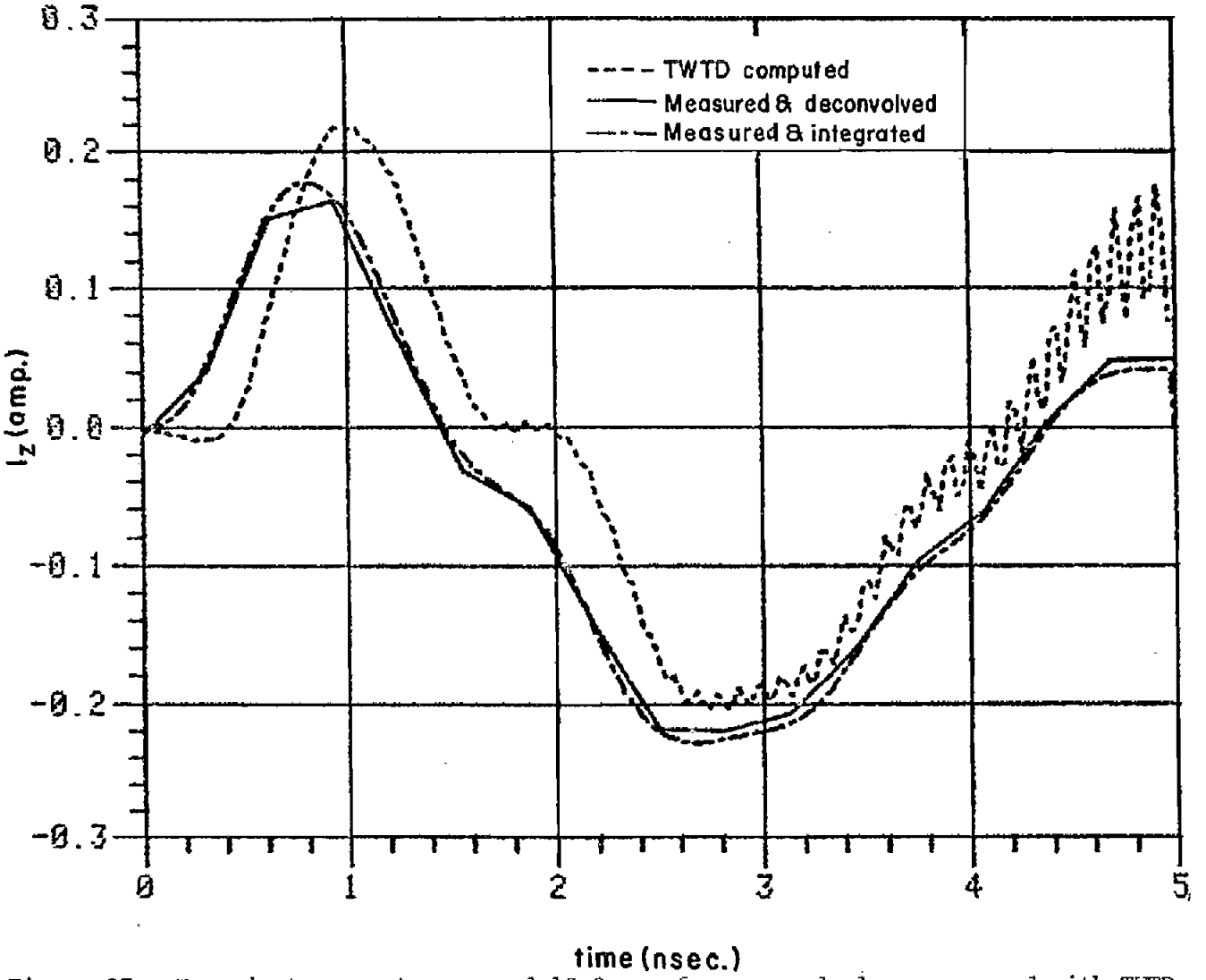

Figure 27. Transient current measured 13.0 cm. from ground plane compared with TWTD computation 13.3 cm. from ground plane.

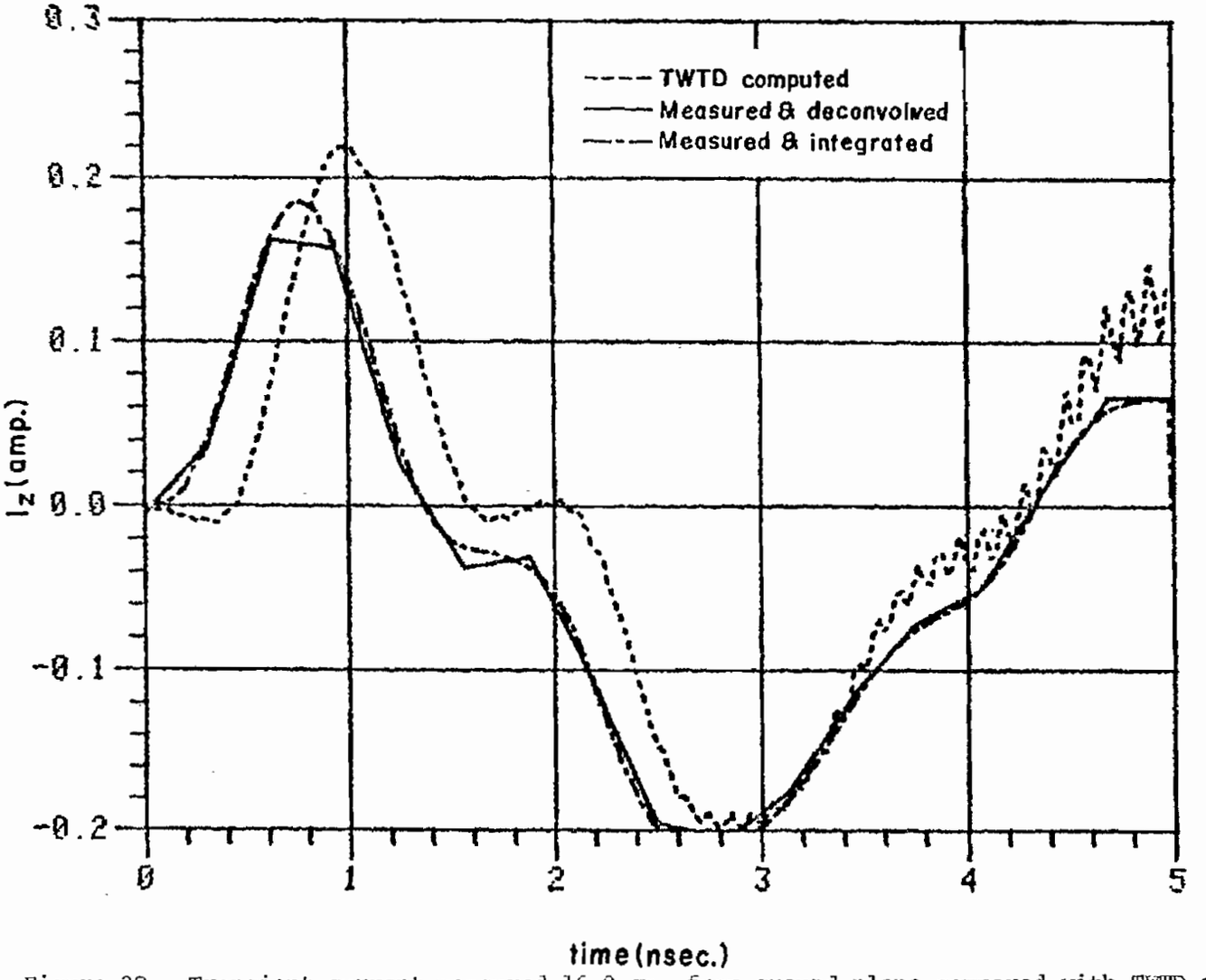

Figure 28. Transient current measured 16.0 cm. from ground plane compared with TWTD computation 15.9 cm. from ground plane.

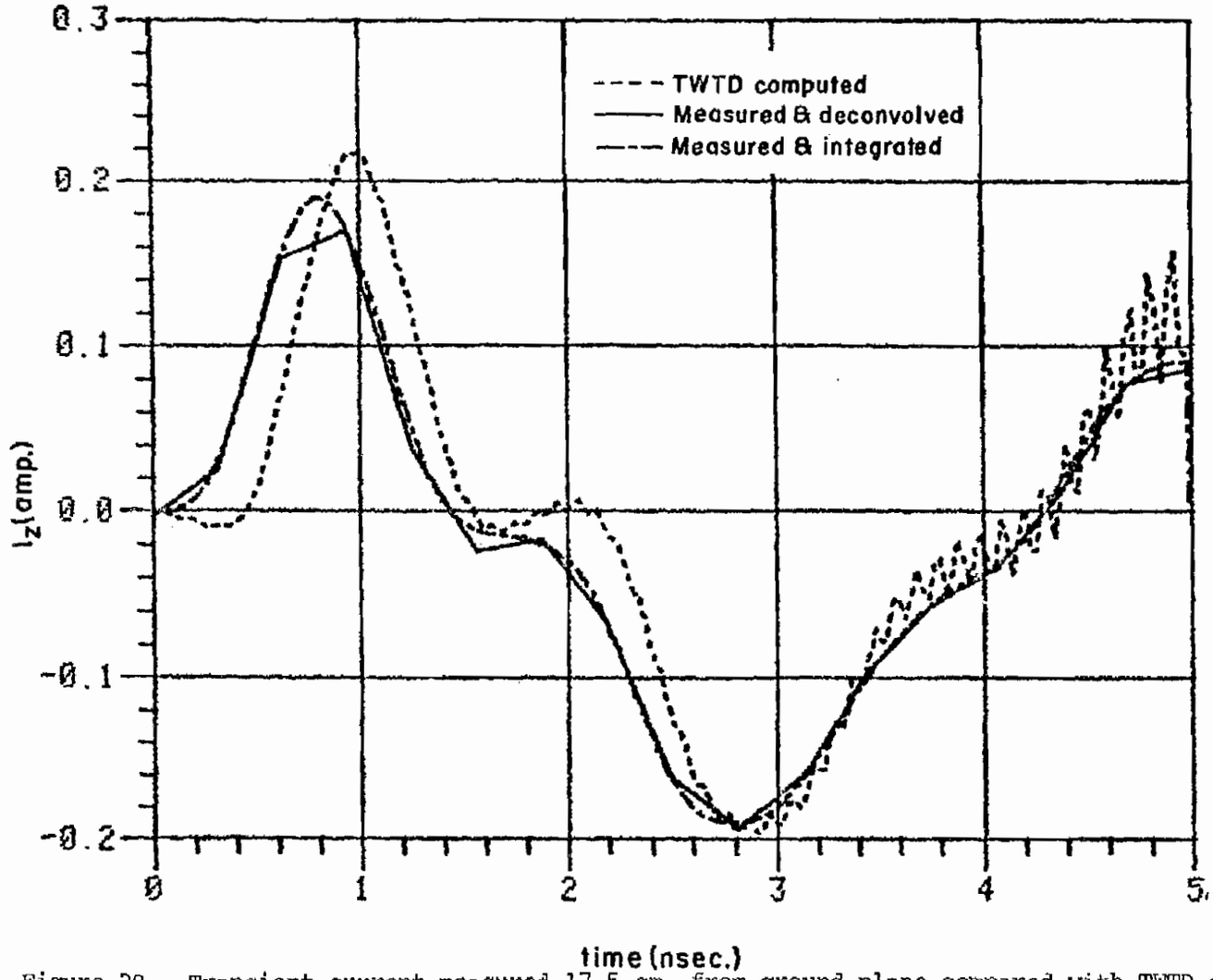

Figure 29. Transient current measured 17.5 cm. from ground plane compared with TWTD computation 17.6 cm. from ground plane.

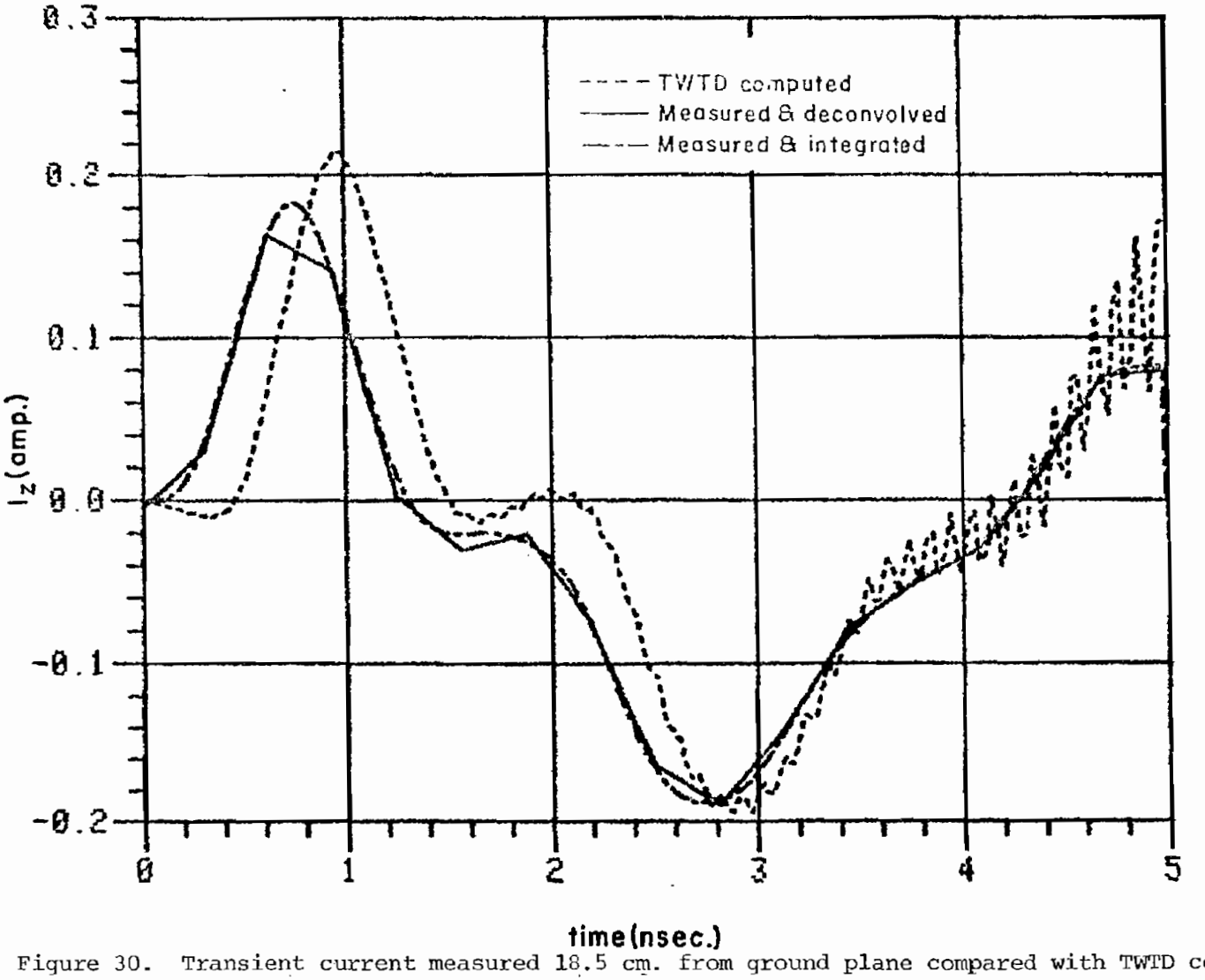

Figure 30. Transient current measured 18.5 cm. from ground plane compared with TWTD computation 18.4 cm. from ground plane.

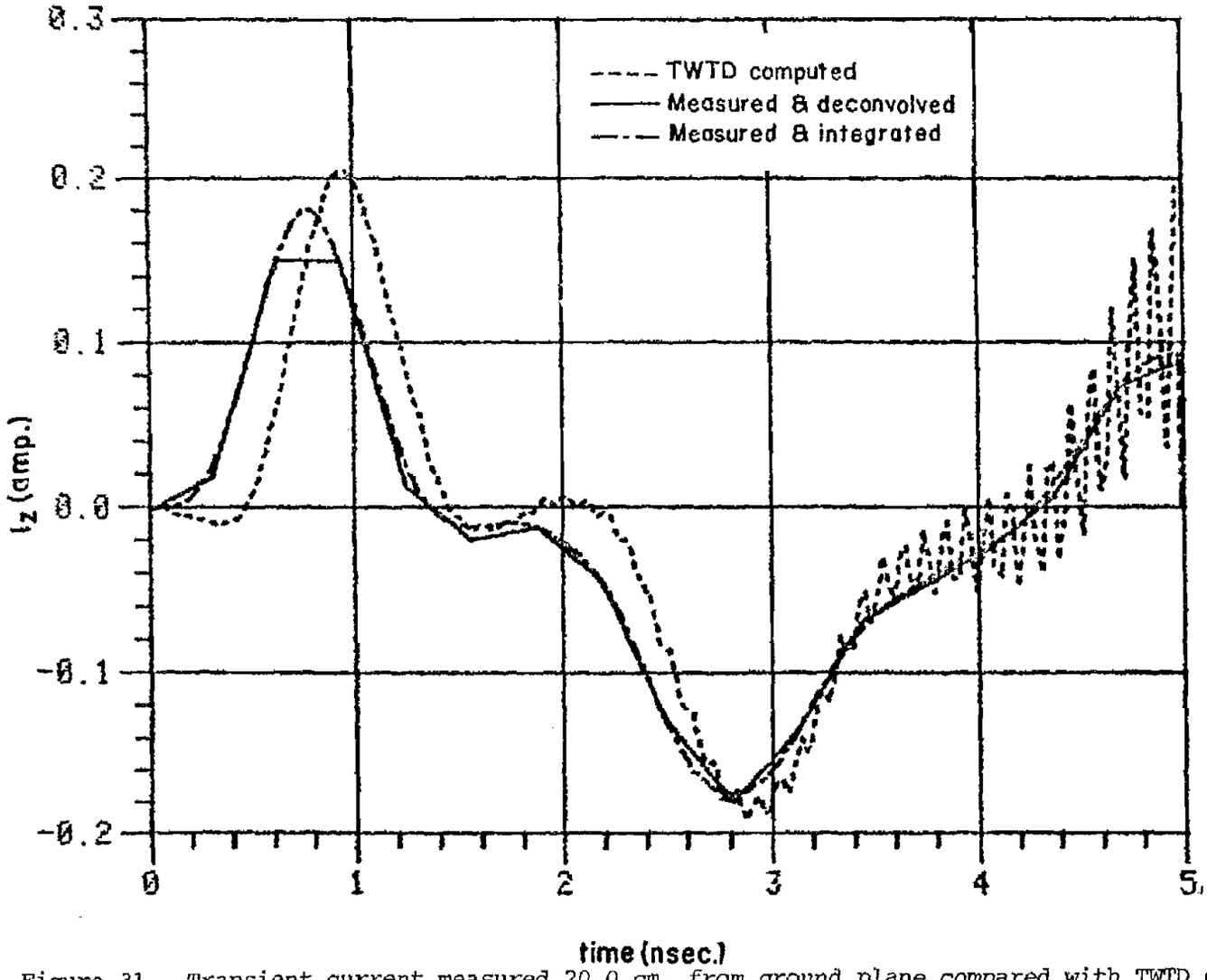

Figure 31. Transient current measured 20.0 cm. from ground plane compared with TWTD computation 20.1 cm. from ground plane.

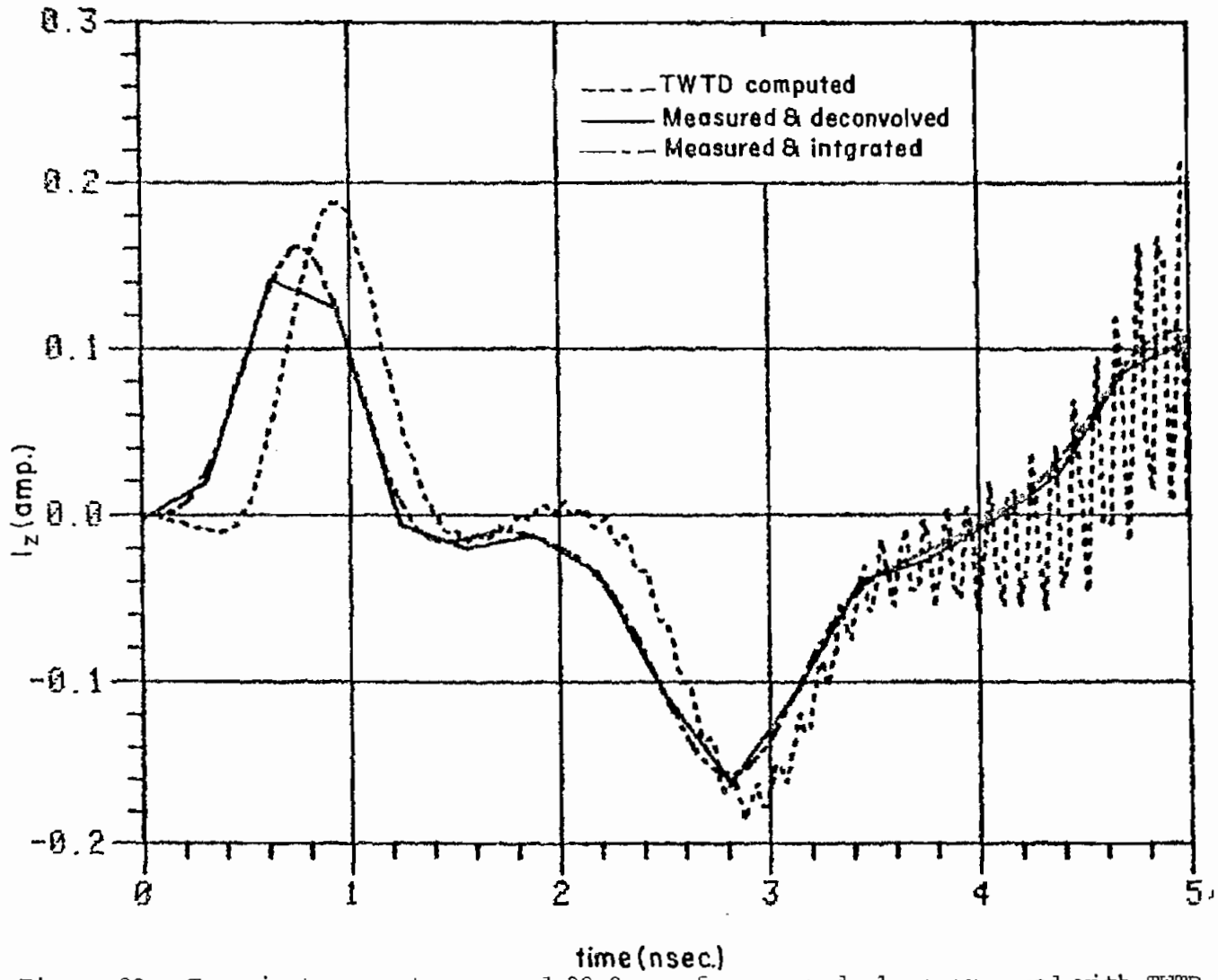

Figure 32. Transient current measured 22.0 cm. from ground plane compared with TWTD computation 21.9 cm. from ground plane.

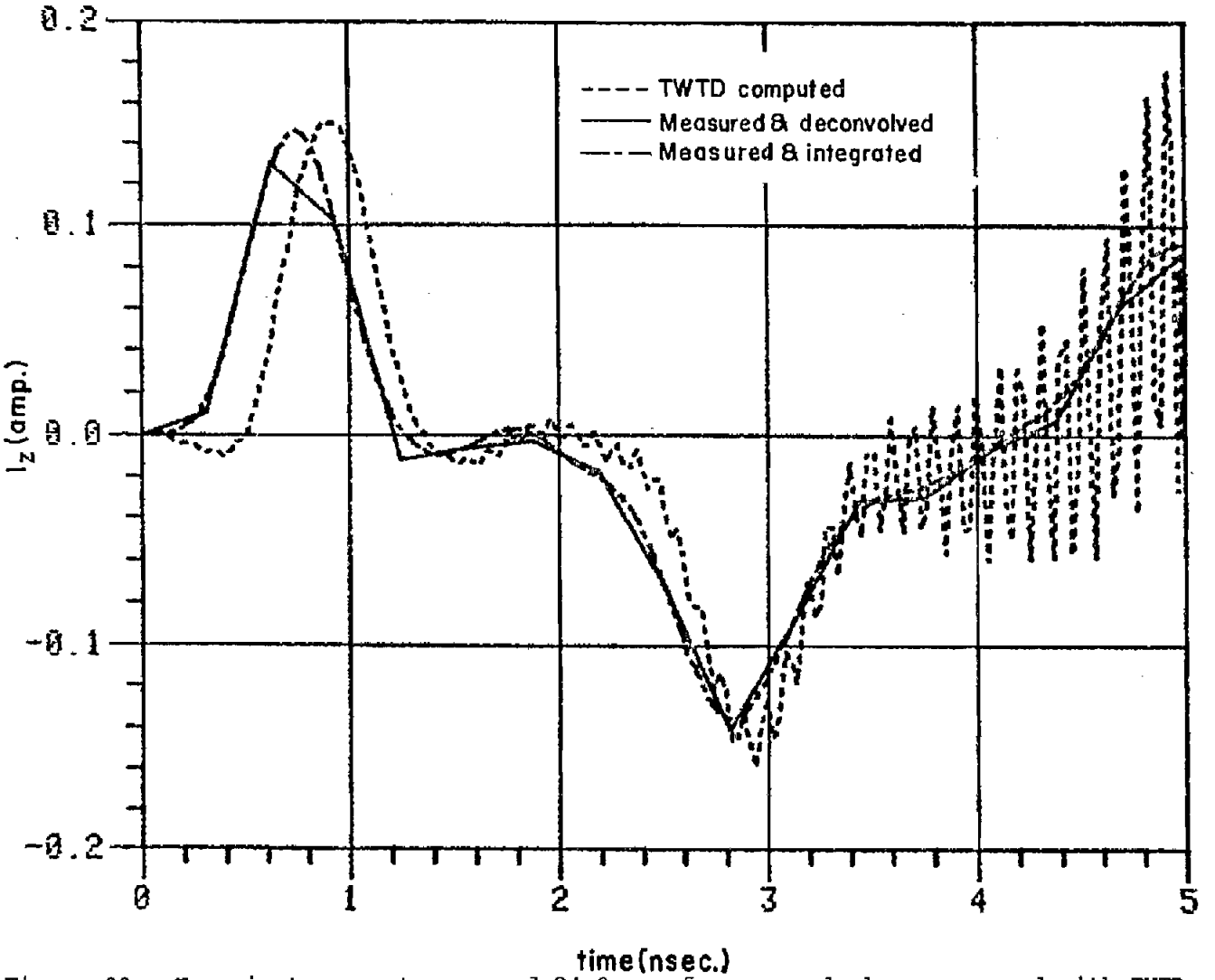

Figure 33. Transient current measured 24.0 cm. from ground plane compared with TWTD computation 24.4 cm. from ground plane.

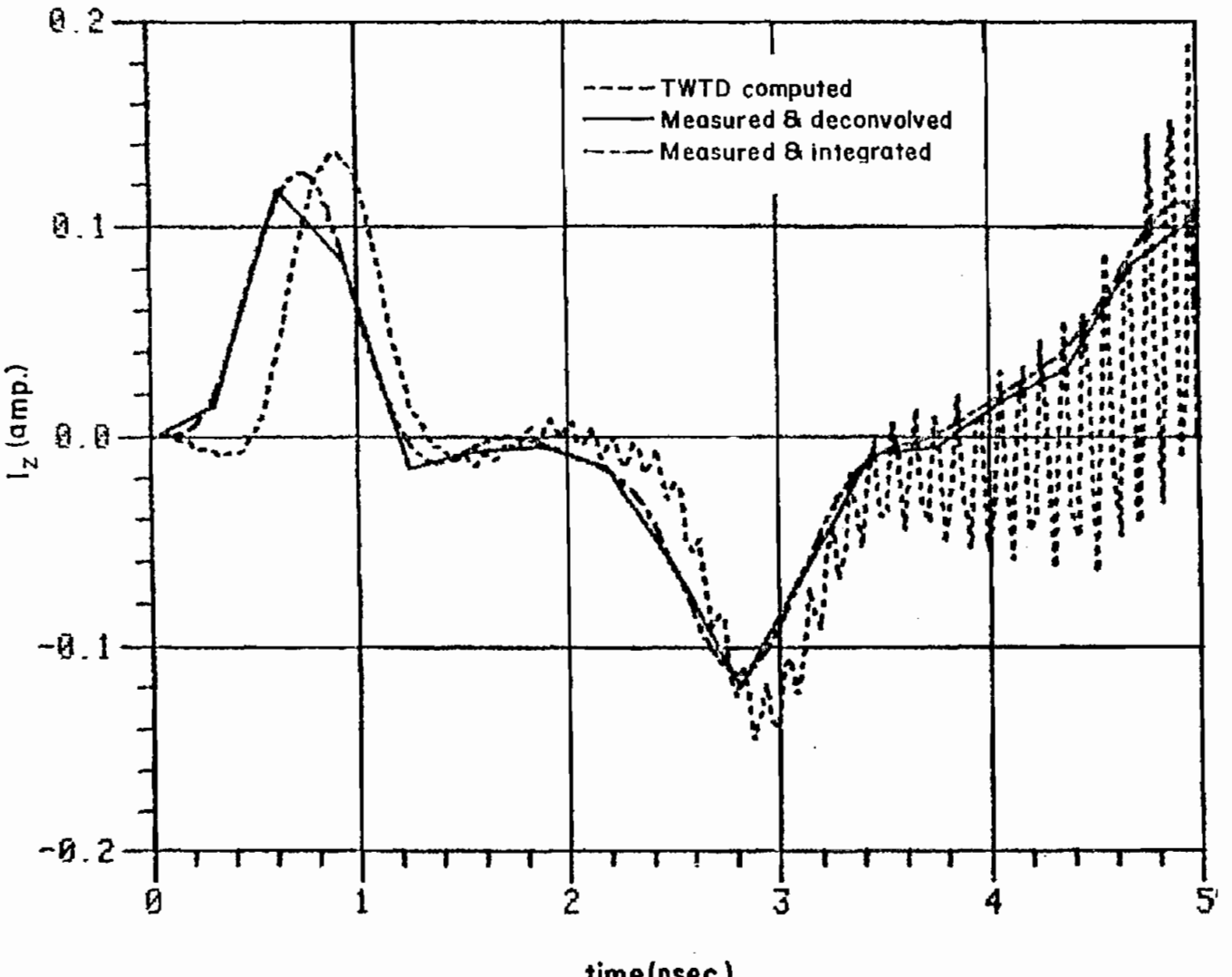

Figure 34. Transient current measured 25.0 cm. from ground plane compared with TWTD computation 25.3 cm. from ground plane.

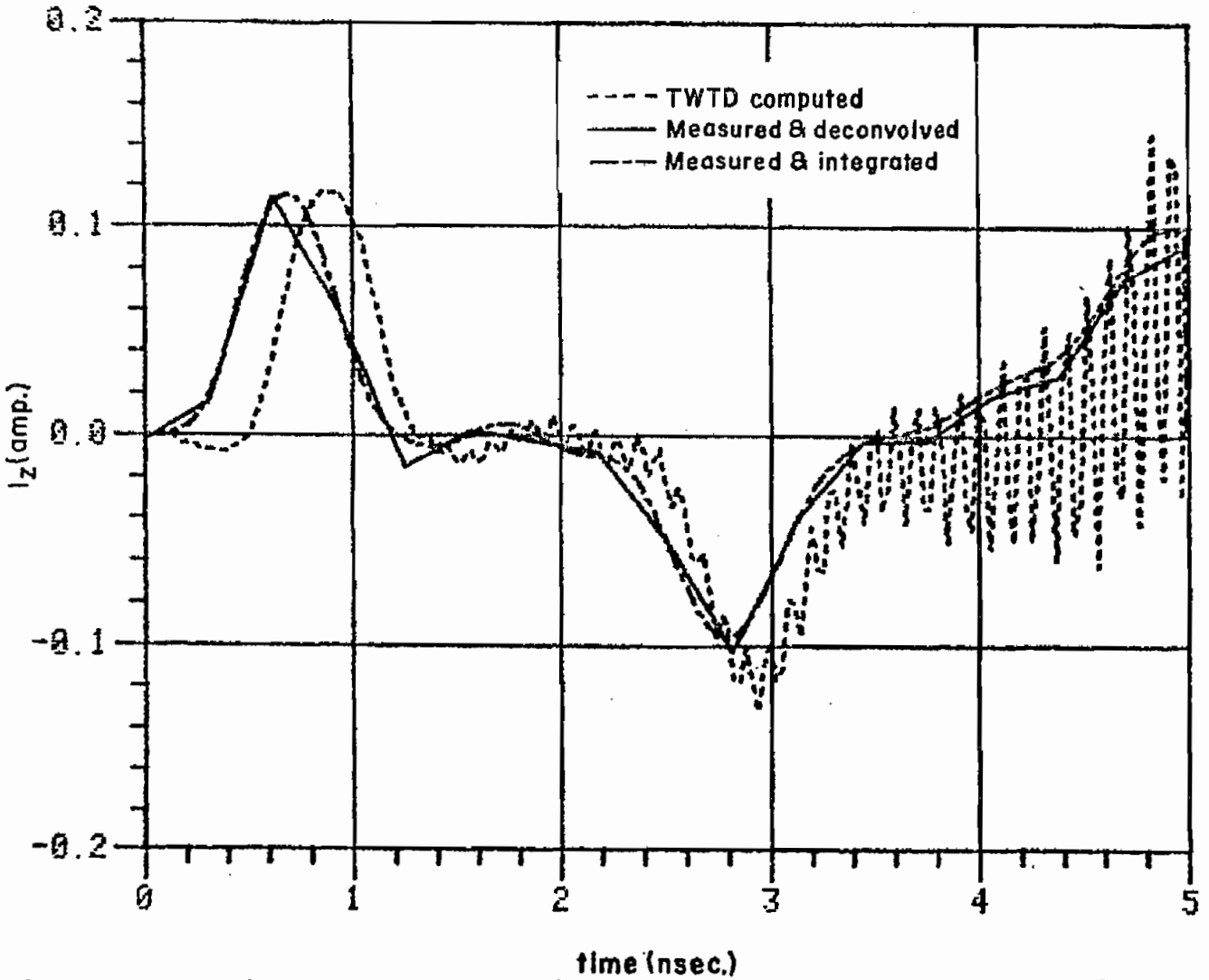

Figure 35. Transient current measured 26.0 cm. from ground plane compared with TWTD computation 26.1 cm. from ground plane.

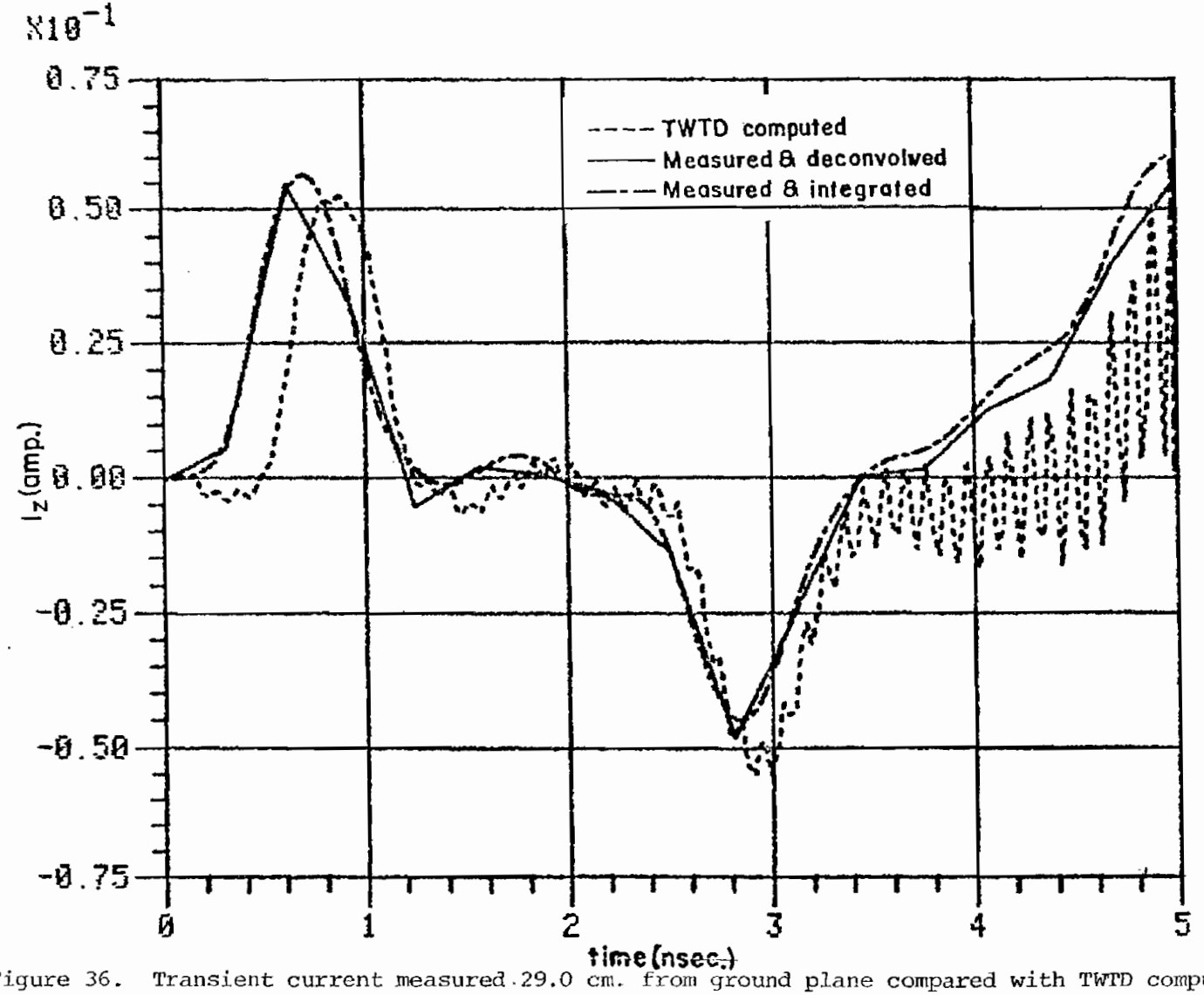

Figure 36. Transient current measured 29.0 cm. from ground plane compared with TWTD computation 28.7 cm. from ground plane.

observation point is further away from the ground plane.

An observation of the comparisons given in Figures 18-36 shows the results to be generally gratifying. The anticipated error in DC level in the measured data is, indeed, observed. The principal features of the waveforms agree well between theory and measurement. The agreement is typical of that obtained in broadband transient experimentation and computation. The quality of agreement is essentially consistent among all of the probe locations. A consistent time shift is apparent throughout the data; namely, the measured data is advanced in time relative to the computed result. This shift is attributable to error in the manually-adjusted time reference in the measurement. This reference was set to the time of initial response at the probe station nearest the ground plane. The use of an electric field probe at the scatterer site for the initial setting of the time reference will likely control this error. The deconvolved results show the effect of rather course quantization resulting from the Fourier transform processing scheme used. This effect may be reduced at the cost of more computation. The integrated results seem to indicate that integration provides adequate probe response deconvolution. The fact that the dominant energy in the pulse spectrum is at frequencies where the probe transfer function is almost a straight line is the reason for this.

3.5 SEM Extraction

In order to determine the SEM description of the cylinder from the measured data, we must extract a set of poles and residues

from the transient data. Natural modes can then be extracted from these poles and residues as described in Reference [1]. In the process of extracting poles, an adaptation of the Pencil-of-Functions method was used in the present work [36]. This pole identifier provides satisfactory pole/residue estimation in the presence of noise in the data.

Extracted natural modes are shown in Figures 37-40 for the first four even-function modes on the cylindrical scatterer. The ground plane symmetry intrinsic to the measurement recovers only the even-function modes. A free-field configuration is required in order to recover odd-function modes. The modes computed by Tesche [31] are provided in the Figures for comparison purposes. These results are for a cylinder with a length-to-diameter ratio of 100. Our scatterer and its image have a length-to-diameter ratio of 63. Tesche demonstrated, however, that the dependence of the modes on the aspect ratio is quite weak.

The agreement between the computed and extracted modes is quite good for the first three even-function modes. The fourth, however, demonstrates only hints of agreement. At least the proper oscillatory features are present. An inspection of the spectrum of the excitation function shown in Figure 9 indicates that the excitation for this mode, which is resonant nominally at 1.75 GHz, is roughly 15 dB below that of the excitation at the 250 MHz fundamental resonance. It is surprising that anything at all is recoverable for such a weakly-excited mode.

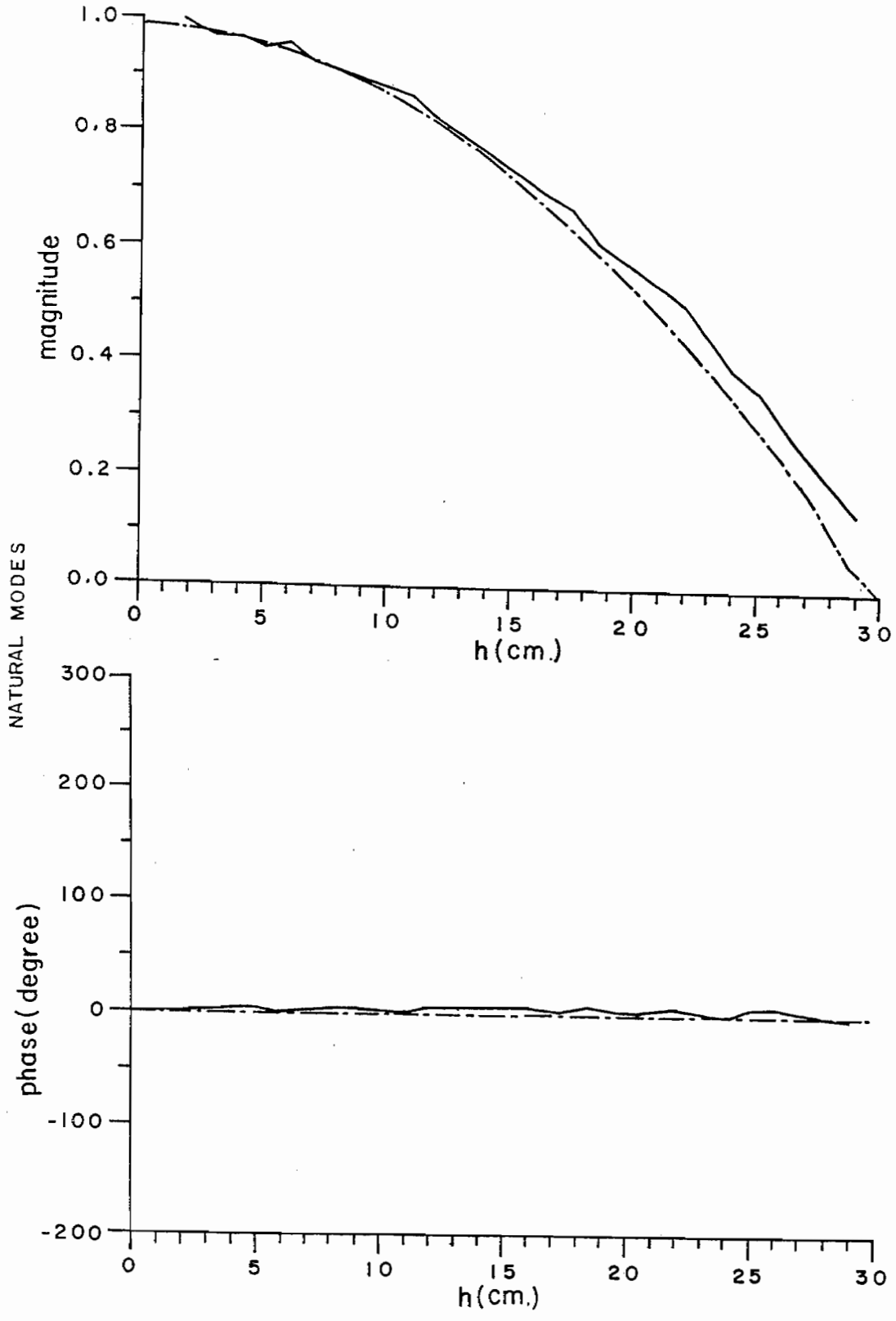

Figure 37. Magnitude and phase plots of natural mode 1 from measured data (solid line) and compared with that of Tesche (dot-dashed line).

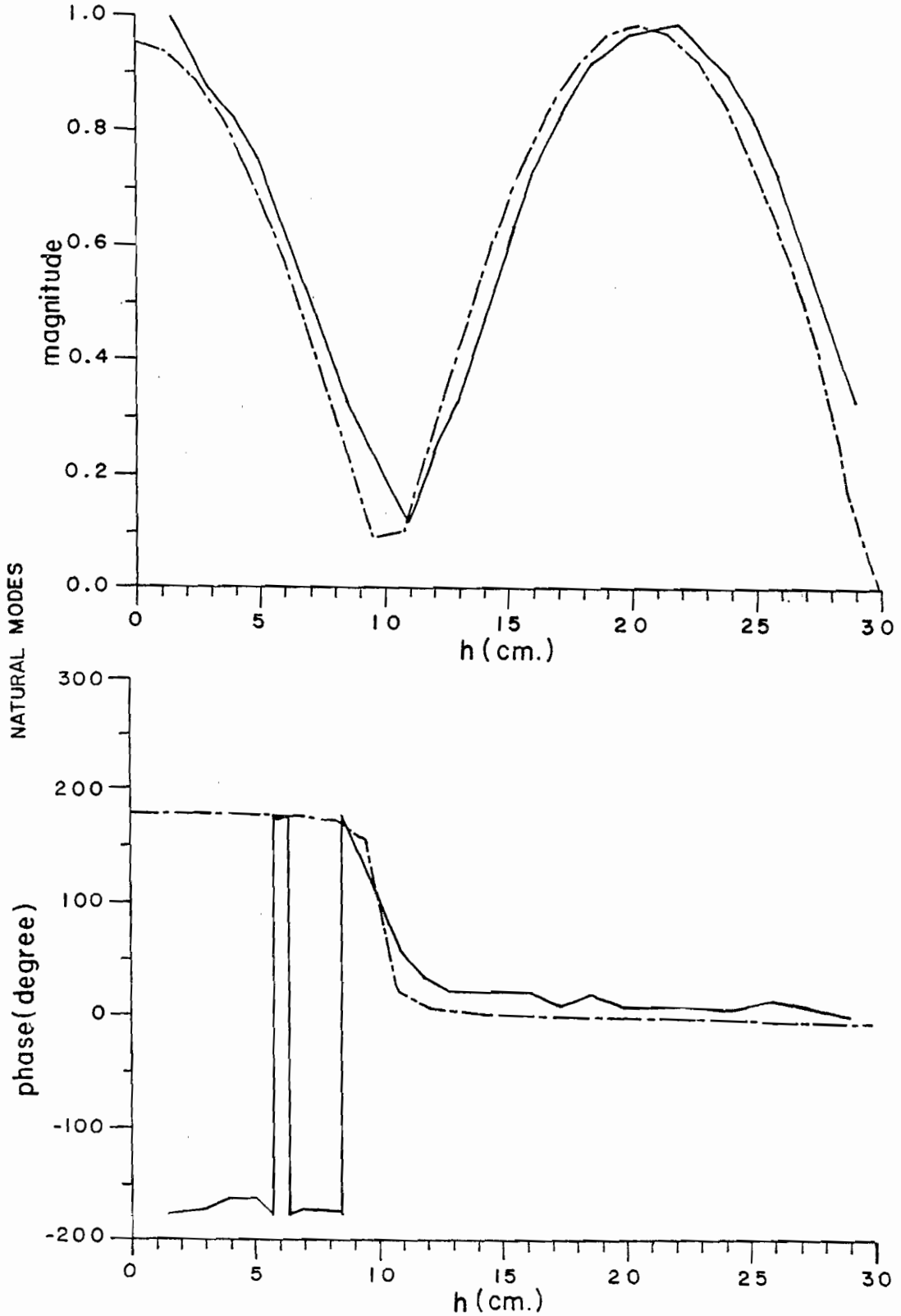

Figure 38. Magnitude and phase plots of natural mode 3 from measured data (solid line) and compared with that of Tesche (dot-dashed line).

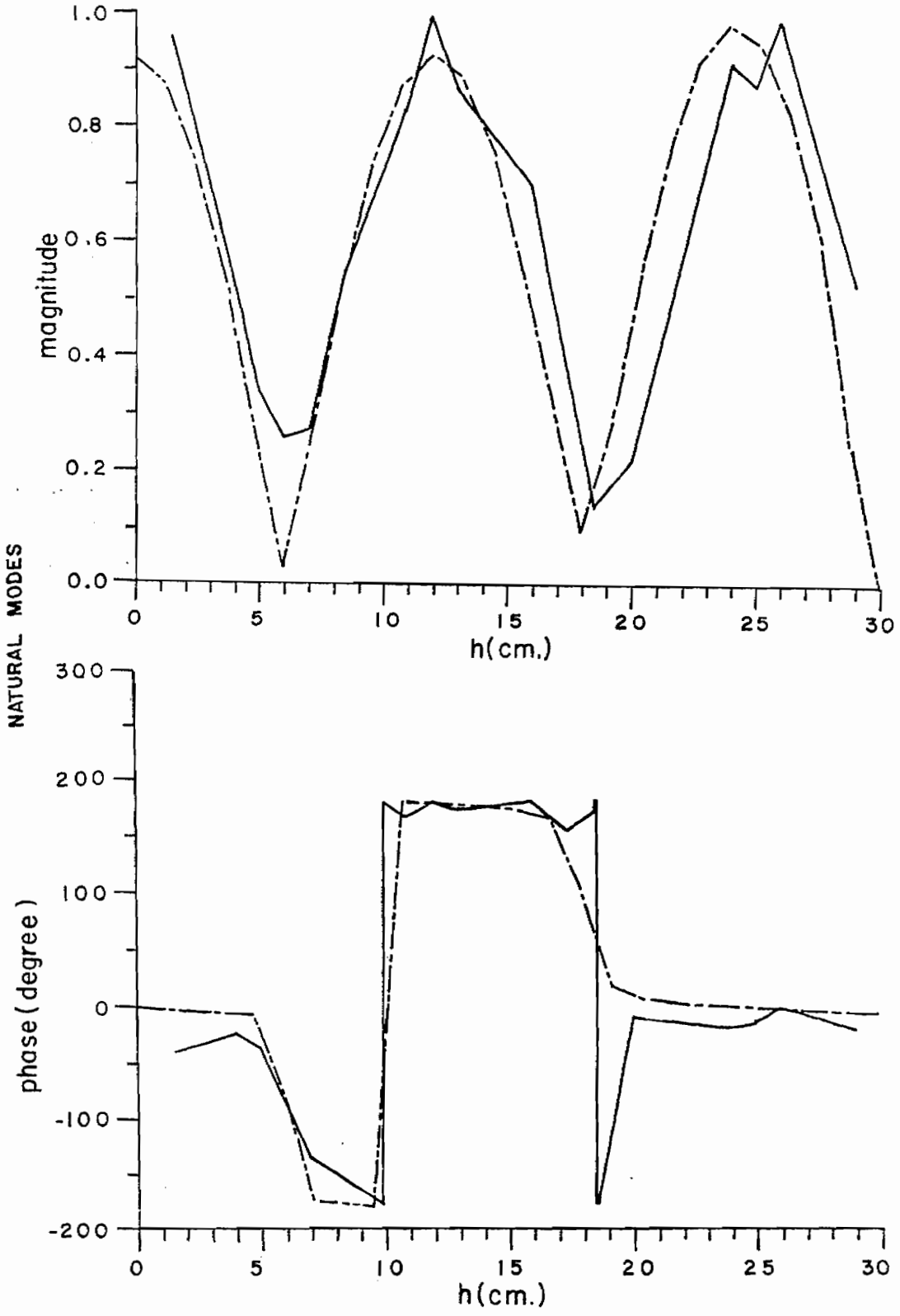

Figure 39. Magnitude and phase plots of natural mode 5 from measured data (solid line) and compared with that of Tesche (dot-dashed line).

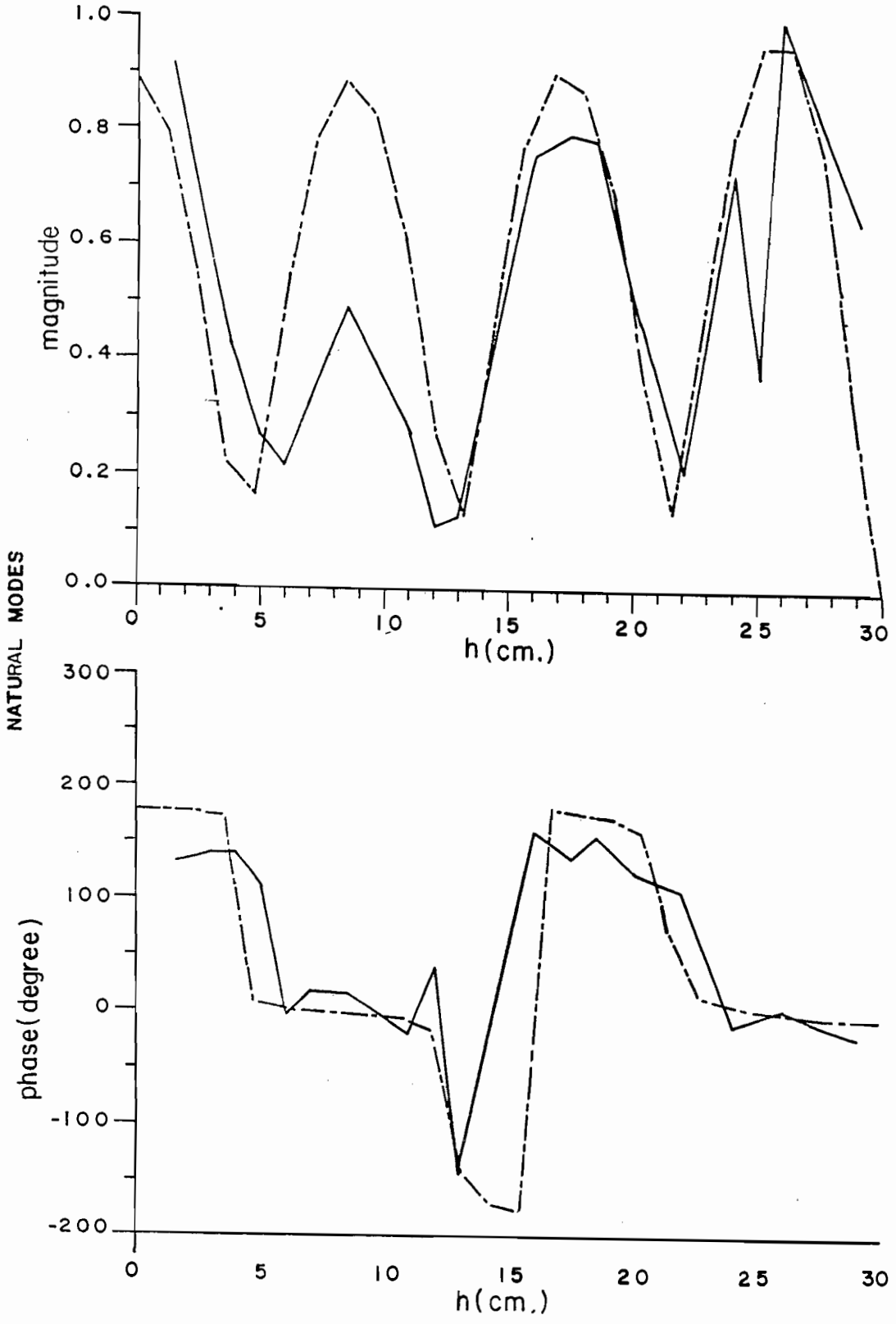

Figure 40. Magnitude and phase plots of natural mode 7 from measured data (solid line) and compared with that of Tesche (dot-dashed line).

IV. CONCLUSION

It appears very feasible to probe the transient surface current on a scatterer using the current probe discussed in this work. The scheme has several advantages. First, this probe is economical since it can be built within a day of labor and without sophisticated equipment. Second, it has satisfactory sensitivity and can sense a reasonably small signal. Third, we can mount this probe on a track so that it can be moved along the object for many structures of interest, therefore eliminating the need of multiple probes. Fourth, it is small in size so that we can readily apply conventional circuit theory in the analysis of the probe. Finally, it shows a fairly broad frequency response (from 0 to about 2.0 GHz). The economy of fabrication is likely to be especially important in probing complex shapes which demand multiple probes rather than movable ones.

On complex shapes such as aircraft the moving-probe scheme is precluded. The use of multiple probes introduces the new problem of relative calibration. The present work, by design, allowed the calibration of the probe on a cylindrical conductor identical in curvature to the scatterer on which it was used. This cannot be accomplished when complex surface shapes are involved. The most appropriate choice of calibration environment is likely to be on a planar surface. The production of a known current on a planar surface is difficult, however. It is quite likely that simply using the theoretical response of the probe and its feed cable will be as reliable as

any calibration in light of the comparisons given in Figure 13. The length of the feed cable may be measured accurately using time domain reflectometry, so that its attenuation and phase responses can be accounted for.

The use of ground plane symmetry, while simplifying the experimental configuration, provides only one of the two sets of modal symmetries on a symmetric object. It is desirable to develop means whereby the method can be implemented on a whole object suspended in air so that all modes are recoverable.

Finally, the SEM modes extracted indicate that the measured extraction scheme proposed in [1] is feasible. The extraction of normalization constants, which complete the SEM description, has not been considered here. Extraction of this parameter will place additional demands on the measured data. In particular, we can anticipate a systematic error in the phase of all of these parameters due to the time-reference error apparent in Figures 18-36. This error in time of arrival is likely to be inconsequential.

APPENDIX

CONSTRUCTION TECHNIQUE FOR CURRENT PROBE

We describe here the fabrication method used for the probes in the hope of saving the interested reader some hours of frustration. Drawings are given for the special tooling involved. The principal steps in the fabrication are 1) bending the loop, 2) cutting the feed gap, and 3) soldering the loop into the carriage.

Figure 41 shows a mandrel designed for bending the loop. In order to make a 0.125 inch diameter semicircular loop as a probe with 0.023 inch semirigid coaxial cable, it is wise to start bending the coaxial cable with somewhat larger loop diameter and slowly reducing the diameter of the loop to the 0.125 inch size, using the mandrel pictured in Figure 41.

Figure 42 shows a tool made to guide a file which is used to notch the outer conductor at the center of the loop. Figure 43 shows the file employed in notching the loop. One should obtain as fine a tooth pattern as possible on a so-called Swedish file and grind the flats to the dimensions given, leaving the teeth on the edges unmarred. The now U-shaped coaxial cable section is placed in the notching jig with the sides of the U in the slots with the semicircle protruding above the central slot. A thin rectangular plate is placed on top of the jig to hold the loop in the slots and clamped in place with a spring clip. A very thin stripe is drawn at the center of the loop around the cable at the location of the intended notch with ink such that color can be distinguished from

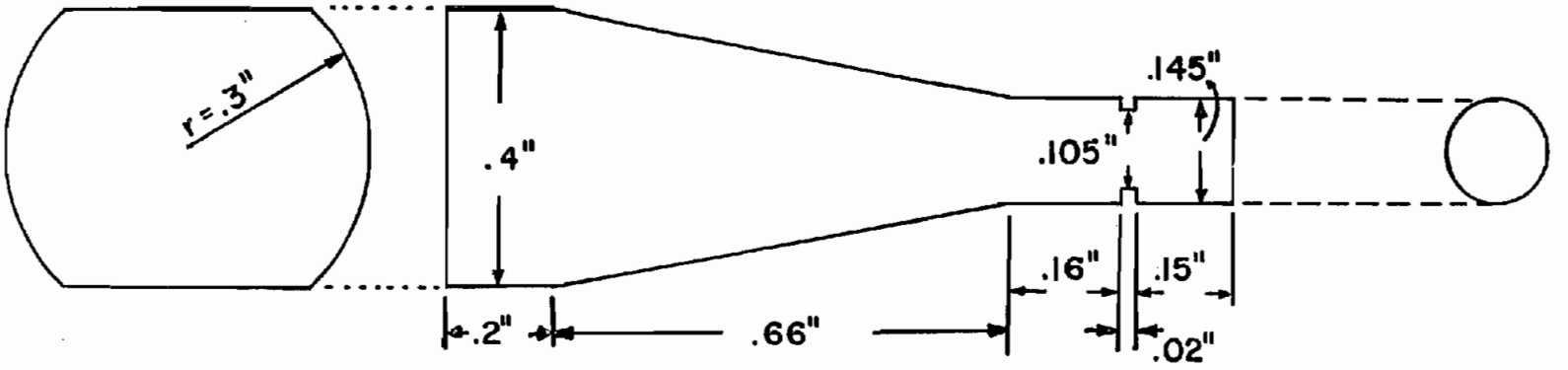

Figure 41. A jig used to make semicircular loop with 0.125" diameter.

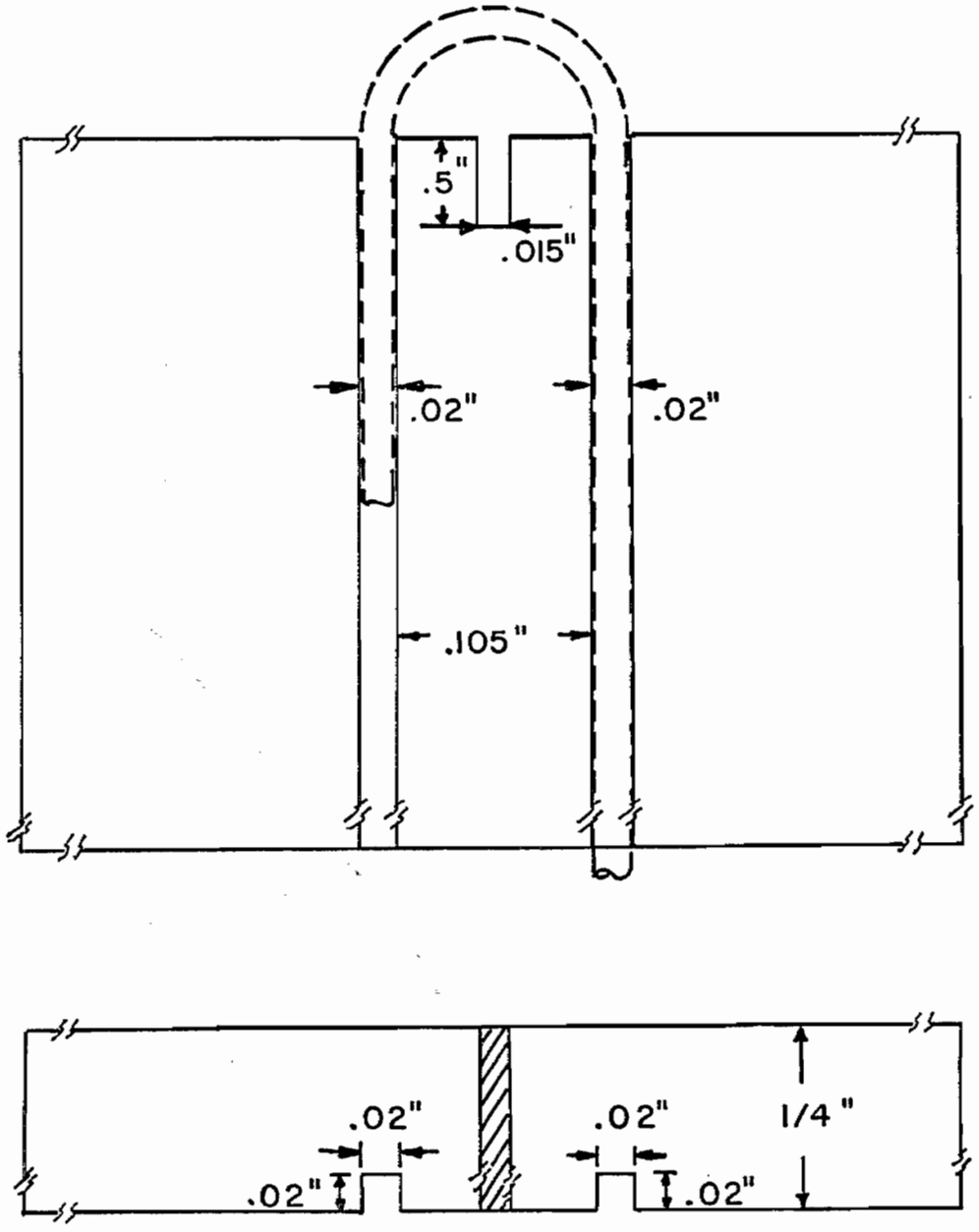

Figure 42. A notching jig to guide a file to notch the center of the probe for three different sizes.

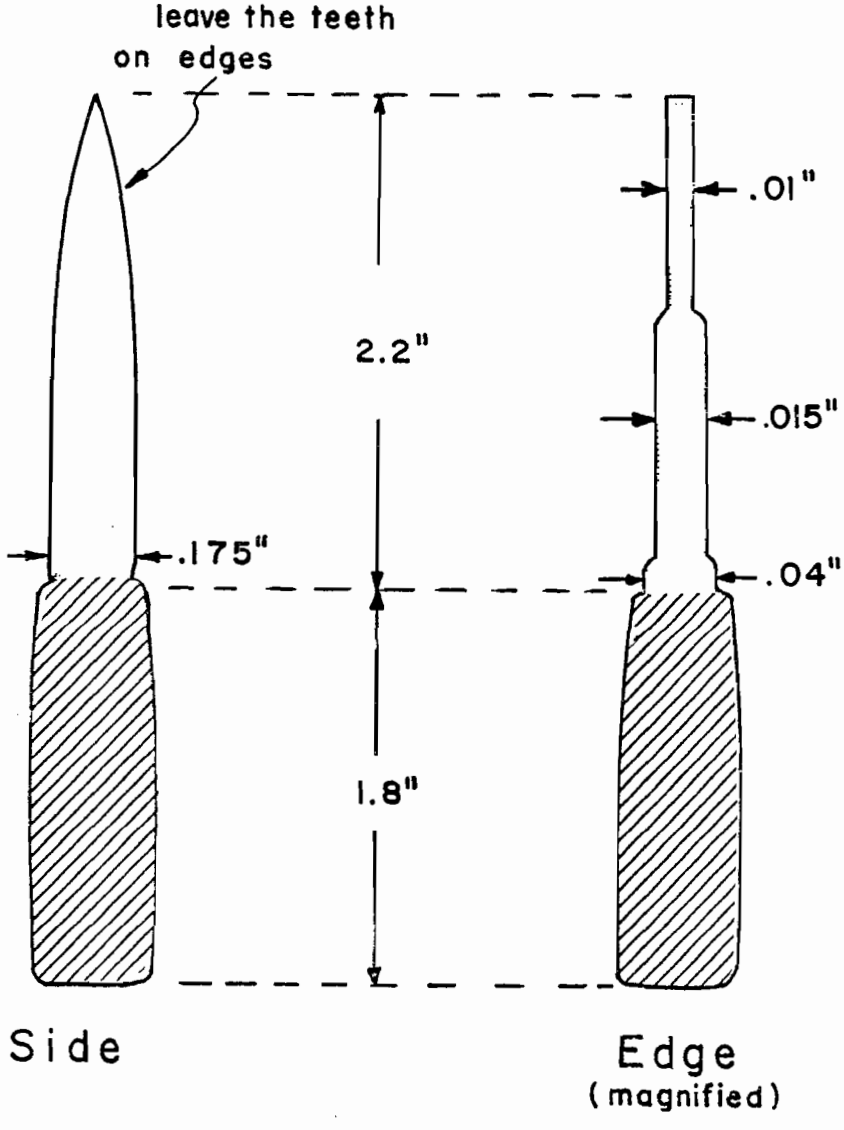

Figure 43. A modified file to notch the semicircular loop. Note: Not scaled.

the copper and teflon. The outer conductor is notched by lightly filing without pressing the cable. Placing a finger against the loop provides support and helps to keep the file from slipping. A jeweler's magnifying headpiece is very helpful in notching the outer conductor, and the notching jig can be clamped in a vise for firm support.

The terminated leg of the loop is cut to length, leaving a few millimeters of the center conductor exposed. The loop is inserted into the carriage, as shown in Figure 2. A 0.105 inch diameter semi-circular key is useful in setting the height of the protrusion. In soldering the loop in place, the prolonged use of heat should be avoided. The Teflon dielectric extrudes when overheated. The center conductor on the terminated end should be soldered to the carriage and the outer conductor. The cable end of the loop is fed through the pushrod tubing and fitted with an Omni Spectra OSSM 551-1 connector, or the equivalent, using the adaptation shown in Figure 4. This connector is soldered to the pushrod for mechanical strength.

REFERENCES

1. Pearson, L. W. and D. R. Roberson, "The Extraction of the Singularity Expansion Description of a Scatterer from Sampled Transient Surface Current Response," IEEE Transactions on Antenna and Propagation, Vol. AP-26, no. 2, March, 1980.

2. Partridge, R. E., "'Invisible' Absolute E-Field Probe," Electromagnetic Pulse Sensor and Simulation Notes, Vol. 1, Note 2, Air Force Weapons Laboratory, June 1970.

3. Partridge, R. E., "Combined E and B-dot Sensor," Electromagnetic Pulse Sensor and Simulation Notes, Vol. 1, Note 3, Air Force Weapons Laboratory, June 1970.

4. Orsak, L. E. and A. L. Whitson, "Electric Field Sensor for EMP Simulators," Electromagnetic Pulse Sensor and Simulation Notes, Vol. 1, Note 18, Air Force Weapons Laboratory, June 1970.

5. Hall, C. J., "The Asymmetric Dipole as a Transient Field Probe," Electromagnetic Pulse Sensor and Simulation Notes, Vol. 9, Note 115, Air Force Weapons Laboratory, June 1971.

6. Baum, C. E., "Two Types of Vertical Current Density Sensors," Electromagnetic Pulse Sensor and Simulation Notes, Vol. 2, Note 33, Air Force Weapons Laboratory, July 1971.

7. Baum, C. E., "Some Considerations for Electrically-Small Multi-Turn Cylindrical Loops," Electromagnetic Pulse Sensor and Simulation Notes, Vol. 2, Note 43, Air Force Weapons Laboratory, July 1971.

8. Baum, C. E., "Some Considerations for Inductive Current Sensors," Electromagnetic Pulse and Simulation Notes, Vol. 4, Note 59, Air Force Weapons Laboratory, June 1970.

9. Baum, C. E., "The Circular Flush-Plate Dipole in a Conducting Plane and Located in Non-Conducting Media," Electromagnetic Pulse Sensor and Simulation Notes, Vol. 7, Note 98, Air Force Weapons Laboratory, June 1970.

10. Baum, C. E., "Characteristics of the Moebius Strip Loop," Electromagnetic Pulse Sensor and Simulation Notes, Vol. 1, Note 7, Air Force Weapons Laboratory, June 1970.

11. Baum, C. E., "Maximizing Frequency Response of a B-Dot Loop," Electromagnetic Pulse Sensor and Simulation Notes, Vol. 1, Note 8, Air Force Weapons Laboratory, June 1970.

12. Baum, C. E., "Electric Field and Current Density Measurements in Media of Constant Conductivity," Electromagnetic Pulse Sensor and Simulation Notes, Vol. 1, Note 13, Air Force Weapons Laboratory, June 1970.

13. Baum, C. E., "Radiation and Conductivity Constants on the Design of a Dipole Electric Field Sensor," Electromagnetic Pulse Sensor and Simulation Notes, Vol. 1, Note 15, Air Force Weapons Laboratory, June 1970.

14. Baum, C. E., "A Technique for Measuring Electric Fields Associated with Internal EMP," Electromagnetic Pulse Sensor and Simulation Notes, Vol. 1, Note 24, Air Force Weapons Laboratory, June 1970.

15. Baum, C. E., "The Multiple Moebius Strip Loop," Electromagnetic Pulse Sensor and Simulation Notes, Vol. 1, Note 25, Air Force Weapons Laboratory, June 1970.

16. Baum, C. E., "The Influence of Radiation and Conductivity on B-Dot Loop Design," Electromagnetic Pulse Sensor and Simulation Notes, Vol. 2, Note 29, Air Force Weapons Laboratory, July 1971.

17. Baum, C. E., "The Single-Gap Cylindircal Loop in Non-Conducting and Conducting Media," Electromagnetic Pulse Sensor and Simulation Notes, Vol. 2, Note 30, Air Force Weapons Laboratory, July 1971.

18. Baum, C. E., "Parameters for Some Electrically-mall Electromagnetic Sensors," Electromagnetic Sensor and Simulation Notes, Vol. 2, Note 38, Air Force Weapons Laboratory, July 1971.

19. Baum, C. E., "The Multi-Gap Cylindircal Loop in Non-Conducting Media," Electromagnetic Pulse Sensor and Simulation Notes, Vol. 2, Note 41, Air Force Weapons Laboratory, July 1971.

20. Baum, C. E., "Design of a Pulse-Radiating Dipole Antenna as Related to High-Frequency and Low-Frequency Limits," Electromagnetic Pulse Sensor and Simulation Notes, Vol. 5, Note 69, Air Force Weapons Laboratory, June 1970.

21. Baum, C. E., "An Equivalent-Charge Method for Defining Geometries of Dipole Antennas," Electromagnetic Pulse Sensor and Simulation Notes, Vol. 5, Note 72, Air Force Weapons Laboratory, June 1970.

22. Baum, C. E., "Electrically-Small Cylindrical Loops for Measuring the Magnetic Field Perpendicular to the Cylinder Axis," Electromagnetic Pulse Sensor and Simulation Notes, Vol. 5, Note 78, Air Force Weapons Laboratory, June 1970.

23. Baum, C. E., "The Circular Parallel-Plate Dipole," Electromagnetic Pulse Sensor and Simulation Notes, Vol. 6, Note 80, Air Force Weapons Laboratory, June 1970.

24. Baum, C. E., "Some Further Considerations for the Circular Parallel-Plate Dipole," Electromagnetic Pulse Sensor and Simulation Notes, Vol. 6, Note 86, Air Force Weapons Laboratory, June 1970.

25. Baum, C. E., "Resistively Loaded Radiating Dipole Based on a Transmission-Line Model for the Antenna," Electromagnetic Pulse Sensor and Simulation Notes, Vol. 6, Note 81, Air Force Weapons Laboratory, June 1970.

26. Baum, C. E., "The Single-Gap Hollow Spherical Dipole in Non-Conducting Media," Electromagnetic Pulse Sensor and Simulation Notes, Vol. 6, Note 91, Air Force Weapons Laboratory, June 1970.

27. King, R. W. P., R. B. Mack, and S. S. Sandler, Arrays of Cylindrical Dipoles, Cambridge University Press, New York, N. Y., 1968.

28. Liepa, V. V., "Surface Field Measurements on Scale Model EC-135 Aircraft," Interaction Application Memo 15, August 1977.

29. Whiteside, H. and R. W. P. King, "The Loop Antenna as a Probe," IEEE Transactions on Antennas and Propagation, Vol. AP-12, May 1964.

30. King, R. W. P., Fundamental Electromagnetic Theory, Dover Publication, Inc., New York, N. Y., Ch. 6, 1963.

31. Tesche, F. M., "Application of the Singularity Expansion Method to the Analysis of Impedance Loaded Linear Antennas," Electromagnetic Pulse Sensor and Simulation Notes, Note 177, May 1973.

32. Van Blaricum, M. L., "A Numerical Technique for the Time-Dependent Solution of Thin-Wire Structures with Multiple Junctions," M. S. Thesis, Electrical Engineering Department, University of Illinois, 1972.

33. Miller, E. K., A. J. Poggio, and G. J. Burke, "An Integro-Differential Equation Technique for the Time Domain Analysis of Thin Wire Structures, Part I: The Numerical Method," J. of Computational Phys., Vol. 12, 1973.

34. Poggio, A. J., E. K. Miller, and G. J. Burke, "An Integro-Differential Equation Technique for the Time Domain Analysis of Thin Wire Structures II: Numerical Results," J. of Computational Phys. 12, 1973.

35. Harrison, C. W., Jr. and R. W. P. King, "On the Transient Response of an Infinite Cylindrical Antenna," IEEE Transactions on Antennas and Propagation, March 1967.

36. Auton, J. R. and L. W. Pearson, "An Adaptive Filtering Algorithm for the Identification of SEM Poles," National Radio Science Meeting, University of Colorado, Boulder, Colorado, November 5-8, 1979.

☆ U. S. GOVERNMENT PRINTING OFFICE 1980 - 678-752/427 Reg. 8